SYNTHESIS AND CHARACTERIZATION OF NOVEL ORGANOMETALLIC-SEMICONDUCTOR NANOCOMPOSIT PHOTOELECTRODES

A Thesis Submitted to
the Graduate School of Engineering and Sciences of
İzmir Institute of Technology
in Partial Fulfillment of the Requirements for the Degree of

DOCTOR OF PHILOSOPHY

in Chemistry

by
Emre Yusuf GÖL

July 2022
İZMİR

ACKNOWLEDGEMENTS

I would like to express my sincere thanks to my advisor Assoc. Prof. Dr. Engin KARABUDAK for his endless support and guidance throughout my Ph.D. thesis. He has always encouraged and helped me with his deepest knowledge, patience, and support. His research motivation, enthusiasm, and knowledge in academia have inspired me not only in my thesis but also in my future career as a chemist. I take this opportunity to thank his for helping me make this thesis possible.

I would also like to express my sincere thanks to the members of our research group for their support, assistance, and friendship.

I would also like to express my sincere thanks to the GÖL family; I would like to express my sincere thanks to my dear father, mother and sister for their unconditional warm love, their endless belief in me, and their financial and moral support. So glad I have you.

Finally, I would like to give my most special thanks to my beloved wife Damla. I have always felt her support throughout the thesis writing process. Her presence made the process easier. So glad I have you.

ABSTRACT

SYNTHESIS AND CHARACTERIZATION OF NOVEL ORGANOMETALLIC-SEMICONDUCTOR NANOCOMPOSIT PHOTOELECTRODES

Studies on novel electrochemical catalyst synthesis for efficient oxygen evolution reaction (OER) attract the attention of researchers. In general, changing of synthesis method and the doping metal affect the electrochemical activities of BSCF. In this work, silver doped $Ba_{0.5}Sr_{0.5}Co_{0.8}Fe_{0.2}O_{3-\delta}$ (BSCF-Ag) perovskite structure is shown to be a better electrocatalyst for oxygen evolution reaction (OER) due to its lower overpotential and extended durability. BSCF structure was synthesized by the EDTA-citric acid method. Appropriate amount of $Ba(NO_3)_2$ and EDTA were dissolved 0.1 M NH_4OH solution. Nitrate salts of other metals were dissolved in distilled water, then mixed with prepared $Ba(NO_3)_2$ solution. The mixture was stirred at 70 °C until gelation occurred. The gelled samples obtained were baked in a drying oven at 250 °C for 24 h before being calcined at 1000 °C for 12 h. To achieve a current density of 10 mA cm^{-2}, BSCF-Ag has required an overpotential of 0.36 V, which is very low compared to BSCF. To determine the stability of BSCF-Ag, continuous chronopotentiometry tests were carried out for 5 h and at a constant current density of 10 mA cm^{-2}. BSCF-Ag was characterized by XRD, SEM, and XPS.

Recent advances in inkjet printing technology for applications relating to heterogeneous catalysis are presented. Catalysts lie at the heart of most chemical reactions where raw materials are converted to value-added products. Therefore, synthesis and immobilization of active catalysts in the reactor are of great importance. Inkjet printing is an additive manufacturing technology introduced recently as a useful method for the fabrication and application of catalysts as a class of functional materials. Inkjet printing provides special features which can be tailored to the design of high-efficient catalytic processes. This thesis presents an overview of the technology along with developments and challenges associated with the combination of inkjet printing and heterogeneous catalysis, such as ink preparation, thin-film properties and real-life applications.

ÖZET

YENİ ORGANOMETALİK-YARI İLETKEN NANOKOMPOZİT FOTOELEKTROTLARIN SENTEZİ VE KARAKTERİZASYONU

Verimli oksijen evrim reaksiyonu (OER) için yeni elektrokimyasal katalizör sentezi üzerine yapılan çalışmalar, araştırmacıların ilgisini çekmektedir. Genel olarak, sentez yönteminin ve doping metalinin değiştirilmesi, BSCF'nin elektrokimyasal aktivitelerini etkiler. Bu çalışmada, gümüş katkılı $Ba_{0.5}Sr_{0.5}Co_{0.8}Fe_{0.2}O_{3-\delta}$ (BSCF-Ag) perovskit yapısının, düşük aşırı potansiyeli ve uzun süreli dayanıklılığı nedeniyle oksijen evrim reaksiyonu (OER) için daha iyi bir elektrokatalizör olduğu gösterilmiştir. BSCF yapısı EDTA-sitrik asit yöntemiyle sentezlendi. Uygun miktarda $Ba(NO_3)_2$ ve EDTA 0.1 M NH_4OH çözeltisi içinde çözüldü. Diğer metallerin nitrat tuzları damıtılmış suda çözülmüş, ardından hazırlanan $Ba(NO_3)_2$ çözeltisi ile karıştırılmıştır. Karışım jelleşme oluşana kadar 70°C'de karıştırıldı. Elde edilen jelleşmiş numuneler, 1000 °C'de 12 saat kalsine edilmeden önce 24 saat 250 °C'de bir kurutma fırınında pişirildi. 10 mA cm^{-2}'lik bir akım yoğunluğu elde etmek için, BSCF-Ag, BSCF'ye kıyasla çok düşük olan 0,36 V'luk bir aşırı potansiyel gerektirmiştir. BSCF-Ag'nin kararlılığını belirlemek için, 5 saat boyunca ve 10 mA cm^{-2} sabit akım yoğunluğunda sürekli kronopotansiyometri testleri yapıldı. BSCF-Ag, XRD, SEM ve XPS ile karakterize edildi.

Heterojen kataliz ile ilgili uygulamalar için mürekkep püskürtmeli baskı teknolojisindeki son gelişmeler sunulmaktadır. Katalizörler, hammaddelerin katma değerli ürünlere dönüştürüldüğü çoğu kimyasal reaksiyonun merkezinde yer alır. Bu nedenle reaktörde aktif katalizörlerin sentezi ve immobilizasyonu büyük önem taşımaktadır. Mürekkep püskürtmeli baskı, bir fonksiyonel malzeme sınıfı olarak katalizörlerin üretimi ve uygulanması için yararlı bir yöntem olarak yakın zamanda tanıtılan bir eklemeli üretim teknolojisidir. Mürekkep püskürtmeli baskı, yüksek verimli katalitik süreçlerin tasarımına uyarlanabilen özel özellikler sağlar. Bu tez, mürekkep hazırlama, ince film özellikleri ve gerçek hayattaki uygulamalar gibi mürekkep püskürtmeli baskı ve heterojen kataliz kombinasyonu ile ilgili gelişmeler ve zorluklarla birlikte teknolojiye genel bir bakış sunmaktadır.

TABLE OF CONTENTS

LIST OF FIGURES vii

LIST OF TABLES viii

CHAPTER 1. INTRODUCTION 1

1.1. The Challenge of a Sustainable Energy Future 1
1.2. The Use of Renewable Energy 2
1.3. From Solar to Fuel 4
1.4. Strategies for Solar Hydrogen 7
1.5. Photoelectrochemical Water Splitting Standard 7
1.6. The Photoelectrochemical Cell 8
1.7. Materials for Semiconducting Photoelectrodes 10
1.8. Defect Chemistry 12
1.8.1. Doping Bimetallic Oxides 13
1.9. Thesis Overview 13

CHAPTER 2. PHOTOELECTROCHEMICAL MEASUREMENTS 15

2.1. Introduction 15
2.2. The Photoelectrochemical Cell 16
2.2.1. Cell Designs 17
2.2.2. Sample and Substrate 19
2.2.3. The Counter Electrode 21
2.2.4. The Reference Electrode 21
2.2.5. The Electrolyte 23

CHAPTER 3. COMBINATORIAL IDENTIFICATION AND OPTIMIZATION OF NEW OXIDE SEMICONDUCTORS 26

3.1. Introduction 26
3.2. Inkjet Printing: Methodology 28
3.2.1. Inkjet Printing Modes 29
3.2.2. Ink Properties and Printing Conditions 30
3.3. Catalyst-Based Ink Development 32
3.3.1. Prerequisites 32

3.3.2. Carrier Solvent 33
3.3.3. Functional Species Precursor 34
3.3.3.1. Catalyst-Based Solutions 34
3.3.4. Additives 35
3.4. Nickel-Based Multi-Metal Oxides 35
3.5. Experimental 37
3.5.1. Materials 37
3.5.2. Methods 37
3.5.2.1. Ink Formulation 37
3.5.2.2. Characterization of Inks 38
3.5.2.2.1 Viscosity Measurements 38
3.5.2.2.2 Surface Tension Measurements 40
3.5.2.3. Calcination of Metal Oxide Catalysts 41
3.6. Results and Discussion 41
3.6.1. SEM Measurements 41
CHAPTER 4. OXYGEN ACTIVATION ON BA-CONTAINING PEROVSKITE MATERIALS 43
4.1. Introduction 43
4.2. Perovskite Oxide Catalysts 44
4.3. Experimental 48
4.3.1. Synthesis of BSCF Perovskite Structure 48
4.3.1.2. Electrochemical Measurements 48
4.3.3. Results and Discussion 49
4.3.3.1 Materials Structure & Morphology 49
4.3.3.2 Oxygen Evolution Reaction Performance 52
CHAPTER 5. CONCLUSION 56
REFERENCES 58

LIST OF FIGURES

Figure **Page**

Figure 1. 1. Area of area that must be covered with solar cells to produce 20 TW of electrical power at 10% efficiency. 3
Figure 1. 2. A future energy triangle is a conceivable possibility. 5
Figure 1. 3. A diagram depicting a photoelectrochemical cell with a semiconducting photoanode and a metal cathode. The associated energy diagram is displayed to the right. 9
Figure 1. 4. Molecular orbital diagram of rutile TiO_2 (Fischer, 1972; Stoyanov, Langenhorst, & Steinle-Neumann, 2007) 11
Figure 2. 1. Example of a conventional photoelectrochemical cell 17
Figure 2. 2. Photoelectrochemical cell used by our group 18
Figure 3. 1. Schematic illustration of drop-on-demand inkjet printing processes: (a) piezoelectric DOD mode and (b) thermal DOD mode. 30
Figure 3. 2. Square prints with inks we have prepared using our own ink formulation Fe, Co, Cr, Cu and Ni inks from top to bottom, respectively. 38
Figure 3. 3. The experimental setup for viscosity measurement of precursor inks. 39
Figure 3. 4. The experimental setup for surface tension measurement of precursor ink 40
Figure 3. 5. SEM images of trimetallic NiFeCo sample. 42
Figure 3. 6. SEM images of trimetallic $Ni_{87}Fe_7Co_6O_x$ sample. 42
Figure 4. 1. ABO_3 type perovskites structures showing A-Site and B sites atoms with oxygen vacancy. 45
Figure 4. 2. XRD patterns of BSCF and BSCF-Ag powders 50
Figure 4. 3. SEM images of a BSCF-Ag and b BSCF perovskite oxides 51
Figure 4. 4. X-ray photoelectron spectroscopy (XPS) spectra of BSCF and BSCF-Ag 52
Figure 4. 5. LSVs for a BSCF and BSCF-Ag and b Tafel plots for perovskite structures between 0.1 and 0.5 mA cm^{-2} 53
Figure 4. 6. Chronopotentiometric measurements of BSCF-Ag and BSCF maintainin a constant current density of 10 mA cm^{-2} in a 1 mol L^{-1} KOH solution .. 54
Figure 4. 7. XPS spectra of Co 2p and Ba 3d for BSCF-Ag and pure BSCF 55

LIST OF TABLES

Table **Page**

Table 1. 1. An overview of the world's renewable energy production capacity (Lewis et al., 2005; Lewis & Nocera, 2006) 3
Table 1. 2. Numerous fuels' gravimetric and volumetric energy densities (at 1 bar)..... 6
Table 2. 1. Typical materials parameters for some common TCOs..... 20
Table 2. 2. Overview of reference electrodes commonly used in PEC research 22
Table 2. 3. Electrical conductivities for various electrolytes and the corresponding electrolyte resistances and voltage drops for a current density of 5 mA/cm^2..... 25
Table 3. 1. Comparison of typical deposition technologies 28
Table 3. 2. Viscosity measurements of catalyst precursor inks. 39
Table 3. 3. Surface tension measurements of catalyst precursor inks. 40
Table 4. 1. Rietveld refined parameters and reliability factors of perovskites..... 50
Table 4. 2. Chemical composition of BSCF-Ag perovskite structures results from the the EDX analyzes 51
Table 4. 3. Summarization of OER performances of BSCF and BSCF-AG perovskite structures. 54

CHAPTER 1

INTRODUCTION

1.1. The Challenge of a Sustainable Energy Future

Providing enough energy to the world's population in order to maintain current living standards is among the most important difficult tasks affecting people all across the world in the twenty-first century. A total of 15 TW of power is consumed by the world's almost 7 billion people as of 2011, and this figure is expected to rise to 9 billion and 30 TW by 2050, according to estimates. This growth in demand will put a strain on our current energy supply, which accounts for around 85 percent of it. Ultimately, this boils down to a matter of resources. Coal, oil, and natural gas all have estimated reserves ranging from 150 to 400 years based on current consumption rates. Shorter-term effects will be felt due to diminishing stocks. Due to the fact that the supply will run out before the reserves are used, the peak production will occur long before the stocks are depleted. Oil manufacturing of conventional (easily recoverable) type has already reached its peak, according to information provided by the International Energy Agency, in 2006. There's no chance of it ever returning to its pre-2001 (inflation-corrected) level, considering the price of oil has climbed considerably since 2001.

The environmental impact of fossil fuel consumption may be a considerably more significant worry than the use of fossil fuels themselves. One of the most pressing issues here is the increase in greenhouse gas emissions, particularly carbon dioxide (CO_2). The CO_2 level in the atmosphere has risen from 280 to 394 ppm since the beginning of the industrial revolution, and it is currently rising by roughly 2 ppm/year. Global warming of more than 2°C is possible if CO_2 levels rise above 450 ppm, according to the International Panel on Climate Change. Climate change is expected to have a long-term negative influence on ecosystems and human society if it continues to grow. Society has a reasonable chance of adapting if the increase in temperature is kept to less than 2°C. This decade, from 2010 to 2020, is regarded by many as significant. If we do not drastically reduce CO_2 emissions during the next decade, it appears that we will breach the 450-ppm limit (Allison et al., 2009; Oppenheim & Beinhocker, 2009).

Our reliance on fossil fuels must be phased out in order to cut CO_2 emissions and lower our carbon footprint. Uncertainty still abounds, however, as the majority of scientists and policymakers now agree that such a change is unavoidable. A route's viability is frequently influenced by factors other than technological ones, such as cost. For the photoelectrochemical water splitting technique that is the subject of this thesis, cost is a major element.

A perhaps far more serious concern associated with the use of fossil fuels is the impact on the environment. The main concern in this regard is the emission of greenhouse gases, in particular CO_2, and their contribution to global warming. Since the beginning of the industrial revolution, the CO_2 level in the atmosphere has risen from 280 to 394 ppm, and it is currently rising by about 2 ppm/year. According to the International Panel on Climate Change (IPCC), a CO_2 level above 450 ppm carries a high risk of causing global warming by more than 2 °C. Such a rise is likely to have a severe adverse impact on ecosystems and human society, with effects that will be felt throughout the century. If the temperature change can be limited to less than 2°C, there is a good chance that society can adapt. Several studies agree that the current decade, between 2010 and 2020, is a critical one. Unless we can sharply reduce CO_2 emissions within the next 10 years, exceeding the 450-ppm level seems unavoidable.

1.2. The Use of Renewable Energy

While a comprehensive assessment of the many sustainable energy sources and choices is beyond the scope of this chapter, it is useful to consider their estimated worldwide power generation capacities (Table 1.1). Local conditions (geography, climate, population density) will determine the ideal mix of energy infrastructure in the future, which almost definitely includes a combination of these and other technologies. A Terawatt-scale alternative to fossil fuels is unlikely to be implemented within the next few decades because of the enormous effort required. (Hoffert Martin, 2010; Pacala & Socolow, 2004), For at least a few more centuries, the world's estimated total fossil fuel reserves could theoretically support a 25–30 TW energy consumption (Lewis & Nocera, 2006). It will be necessary, however, to use a technique that has not yet been thoroughly tested, to efficiently capture and store CO_2 on a vast scale.

Table 1. 1. An overview of the world's renewable energy production capacity (Lewis et al., 2005; Lewis & Nocera, 2006)

Energy Source	Power (TW)	Remarks
Wind	4	For on- and off-shore installations, it represents 10% to 15% of the worldwide technological potential
Hydroelectric	1 - 2	0.5 TW of untapped potential remains.
Tidal and ocean currents	<2	
Geothermal	12	Only a sliver of this resource can be made use of.
Biomass	10	Switchgrass needs to cover 10% of the Earth's surface.
Nuclear	10	For the next 40 years, a 1-GWpeak power plant must be built every 35 hours. Because of the limited supply of uranium, fast breeder or thorium reactors are required.
Solar	>20	0.16% of the Earth's surface to be covered with 10% effective solar cells to meet this goal. 120,000 Terawatts (TW) of solar energy reaches the Earth's surface per year.

Figure 1. 1. Area of area that must be covered with solar cells to produce 20 TW of electrical power at 10% efficiency.

The only energy source in Table 1.1 that has the ability to supply all of our current and future energy demands is solar power. To generate 20 TW of power from the sun, an area of 816.000 km^2 must be covered with 10% effective solar cells, which is approximately 900 X 900 km^2. The total surface area of France and Germany combined is equivalent to this, even if it appears small when compared to Africa (Fig. 1.1). Even on a global scale, the task of covering such a wide area with solar cells is a formidable one. To put this into perspective, it would take 40 years of continuous production of 650 m2 solar cell panels every second, 24 hours a day, 365 days a year, to generate 20 TW of peak power.

At 35–40 percent each year, the solar cell market is one of the most rapidly expanding in the world today. According to data from the International Energy Agency (IEA), global output of solar cells peaked at 16.6GW peak in 2010. A 3 to 7 TW installed PV capacity is expected by 2050, but no one knows how the industry will develop over the next few decades.

1.3. From Solar to Fuel

The intermittent nature of solar power (due to the day/night cycle and clouds) will become increasingly challenging for electrical network operators to manage as solar energy's share of the total energy mix grows. Large-scale energy storage options will be necessary at some time in the future when grid-based storage capacities are exhausted. Chemical fuel storage as a means of storing solar energy is one of the more appealing options. In many cases, the energy of a visible-light photon, which is measured in kilojoules per molecule (kJ/mol), is more than enough for chemical synthesis. Because of their high energy storage density and portability, chemical fuels outperform other energy storage technologies such as batteries and mechanical or gravity-based devices like flywheels and pumped water reservoirs. Gasoline, diesel, ethanol, and other aliphatic hydrocarbons are examples of chemical fuels, as are hydrogen and methane.

All of these examples, with the exception of hydrogen, necessitate a carbon source. However, extracting CO_2 from the atmosphere, which is an apparent choice due to environmental concerns in Section 1.1, is costly because of its dilute nature. Power facilities based on fossil fuels appear to be enticing sources of highly concentrated CO_2,

but the objective of the exercise was to avoid the use of fossil fuels altogether. Using sunlight as a source of energy to synthesize fuels from CO_2 generated by, for example, automobiles would be a more appealing option. This would end the CO_2 cycle. An issue that needs to be addressed is the energy penalty associated with CO_2 capture. To directly convert CO_2 to a fuel via photo(electro)chemical means, the electrochemical half-reactions for methanol or methane involve difficult six- and eight-electron transfer steps, respectively.

The conversion of solar energy into hydrogen appears to be a far more viable method based on these arguments. Fortunately, water is a readily available and convenient hydrogen source, and there is more than enough to go around. In order to store the amount of energy the world consumes in a year (4.7 X 10^{20} J), a simple calculation shows that 3.5 X 10^{13} L of water is required. This is equivalent to 0.000002 percent of the water in the world's oceans, or 1% of the yearly rainfall. The following is a formula for the water splitting reaction:

$$2H_2O + sunlight \rightleftharpoons 2H_2 + O_2 \; \Delta G = 237 \; kJ/mol. \tag{1.1}$$

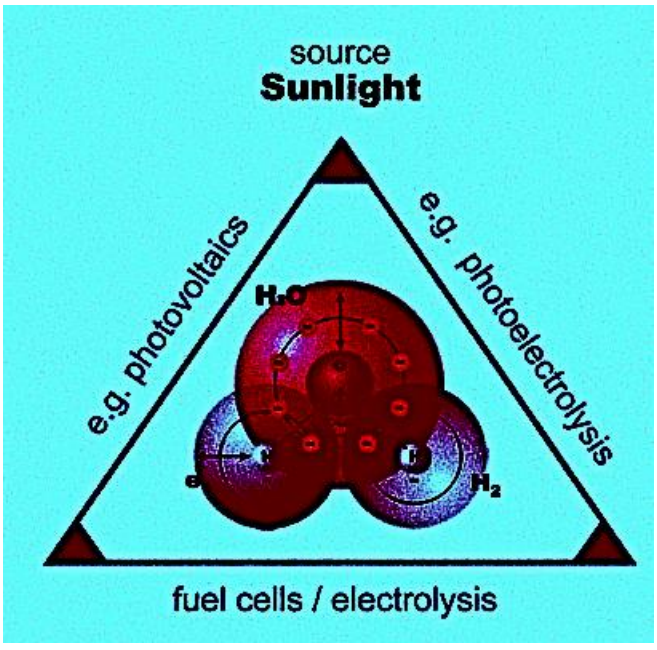

Figure 1. 2. A future energy triangle is a conceivable possibility.

Table 1. 2. Numerous fuels' gravimetric and volumetric energy densities (at 1 bar)

	Energy Density	
Fuel	**Gravimetric (MJ/kg)**	**Volumetric (MJ/L)**
Coal	24	-
Wood	16	-
Gasoline (Petrol)	44	35
Diesel	46	37
Methanol	20	18
Natural Gas	54	0.036
Hydrogen	143	0.011

The reduction half-reaction is a simple two-electron transfer reaction, whereas the oxidation of water to oxygen involves four electrons. It is substantially simpler to photooxidize water than it is to photoreduce CO_2, while neither process is simple. In addition, fuel cells and electrolyzers can easily transform hydrogen into energy and vice versa. As depicted in Fig. 1.2, this presents the possibility of a future energy infrastructure based on sunshine, hydrogen, and electricity.

Hydrogen's difficulty to store is one of the primary difficulties related with it. Hydrogen has a very high gravimetric energy density but a relatively low volumetric energy density (Table 1.2). High-pressure storage containers (up to 700 bar), liquid cryo-storage, physisorption at high-surface area metal organic frameworks (MOFs), and clathrate hydrate cages are also viable options. Alternatively, hydrogen can be stored by creating chemical bonds. This can be accomplished by the use of metal hydrides, such as MgH_2, $LaNi_5H_6$, and $LiBH_4$, or by combining hydrogen and carbon dioxide to create chemical fuels. The latter method is far simpler than photochemical or electrochemical activation of CO_2 directly. CO_2 and hydrogen, for instance, can be transformed to CO through the slightly endothermic reverse water–gas shift reaction:

$$CO_2 + H_2 \rightleftharpoons H_2O + CO \; \Delta H = +42 \; kJ/mol. \tag{1.2}$$

Using well-established Fischer–Tropsch technology, the CO and H_2 (syngas) can be separated by a membrane and transformed to liquid hydrocarbon fuels such as methanol and diesel.

1.4. Strategies for Solar Hydrogen

For the conversion of water and sunlight into hydrogen, numerous pathways exist:

- Photoelectrochemical water splitting
- Photocatalytic water splitting
- Coupled photovoltaic – electrolysis systems
- Thermochemical conversion
- Photobiological methods
- Molecular artificial photosynthesis
- Plasma-chemical conversion
- Mechano-catalytic, magnetolysis, radiolysis, etc.

In their latest works, Rajeshwar and Grimes explore several of these techniques in further depth (Grimes, 2008; Rajeshwar, 2008). This thesis is solely concerned with the first approach on the list: photoelectrochemical water splitting with semiconductor photoelectrodes. There are numerous reasons why this strategy is attractive. Hydrogen and oxygen are created at distinct electrodes, which is one of the major advantages. This eliminates significant safety problems and enables the separation of these gases without incurring a significant energy cost. A second advantage is that the process may be conducted at room temperature, which eliminates the need for large-scale solar concentrators that would restrict its applicability to huge central facilities in sunny locations. A third advantage is that a device for photoelectrochemical water splitting can be made solely from inorganic substances. This provides chemical robustness and durability that is difficult to obtain in biological or organic systems.

1.5. Photoelectrochemical Water Splitting Standard

Notably, the aforementioned advantages for photoelectrochemical (PEC) systems are also relevant to coupled photovoltaic–electrolysis systems. Solar cells, electrolyzers, and dc–dc converters are all commercially accessible, and solar-to-hydrogen efficiency of approximately 8 percent have previously been achieved. This method can thus be regarded as the standard for PEC water splitting. PEC has two possible advantages over PV + electrolysis. The primary benefit is that commercial

electrolyzers require cell voltages of 1.9 V to provide ideal operating current densities of 1 A/cm^2. Since the thermodynamically required potential for water splitting is 1.23 V, this establishes a maximum overall energy conversion efficiency of 65 percent (1.23/1.9) (Khaselev & Turner, 1998). In comparison, the current density at a semiconductor photoelectrode immersed in water is significantly lower (10–20 mA/cm^2), and the necessary overpotential is consequently much lower. A PEC system can be created as a single, monolithic unit, which is the second advantage. This reduces the number of packaging components (frame, glass, connectors, etc.) and may result in substantial cost savings. The crucial benchmark value is, in fact, the cost per kilogram of hydrogen. PV + electrolysis hydrogen production costs are estimated to reach $8/kg, which is far more than the $2–4/kg objective established by the US Department of Energy for future hydrogen production paths. Photoelectrochemical water splitting may provide a path to hydrogen production prices between $3 and $5 per kilogram, which is competitive with existing energy sources.

1.6. The Photoelectrochemical Cell

Figure 1.3 shows a simplified energy diagram of a photoelectrochemical (PEC) cell based on a single photoanode and a metal counter electrode. More complicated configurations that involve photocathodes and/or more than one photoelectrode are discussed at the end of this chapter. The main component of the PEC cell is the semiconductor, which converts incident photons to electron–hole pairs. These electrons and holes are spatially separated from each other due to the presence of an electric field inside the semiconductor, the origin of which is discussed in Sect. 2.5. The photogenerated electrons are swept toward the conducting backcontact and are transported to the metal counter-electrode via an external wire. At the metal, the electrons reduce water to form hydrogen gas. The photogenerated holes are swept toward the semiconductor/electrolyte interface, where they oxidize water to form oxygen gas.

Figure 1.3 illustrates a simplified energy diagram for a photoelectrochemical (PEC) cell with a single photoanode and a metal counter electrode. At the end of this chapter, more complex arrangements involving photocathodes and/or multiple photoelectrodes are addressed. The semiconductor is the primary component of the PEC

cell, which transforms incident photons into electron–hole pairs. These electrons and holes are separated spatially within the semiconductor due to the presence of an electric field. The photogenerated electrons are swept toward the conducting backcontact and transferred via an external wire to the metal counter-electrode. At the metal, the electrons convert water into hydrogen gas by reducing it. The photogenerated holes are swept toward the interface between the semiconductor and the electrolyte, where they oxidize water to produce oxygen gas.

Reduction and oxidation reactions for an alkaline electrolyte can be expressed as For an alkaline electrolyte, the reduction and oxidation reactions can be written as

$$4H_2O + 4e^- \rightleftharpoons 2H_2 + 4OH^- \; E^0_{red} = -0.828\, V\; vs. NHE \tag{1.3}$$

$$4OH^- + 4h^+ \rightleftharpoons 2H_2O + O_2 \; E^0_{ox} = -0.401\, V\; vs. NHE \tag{1.4}$$

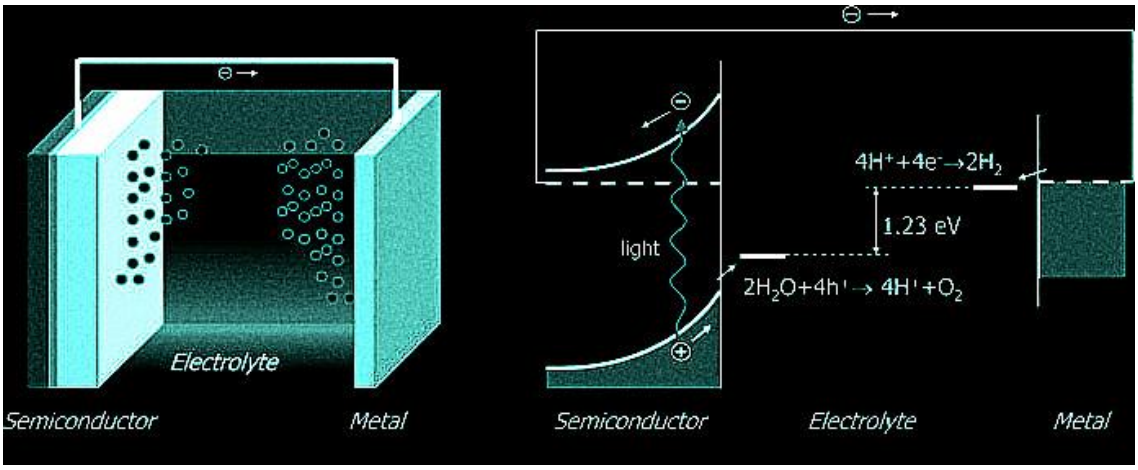

Figure 1. 3. A diagram depicting a photoelectrochemical cell with a semiconducting photoanode and a metal cathode. The associated energy diagram is displayed to the right.

The proper reactions for an acidic environment can be derived from (1.3) and (1.4) by subtracting or adding the dissociation reaction of water into protons and hydroxyl ions:

$$4H^+ + 4e^- \rightleftharpoons 2H_2 \; E^0_{red} = +0.000\, V\; vs. NHE \tag{1.5}$$

$$2H_2O + 4h^+ \rightleftharpoons 4H^+ + O_2 \; E^0_{ox} = -1.229\, V\; vs. NHE \tag{1.6}$$

The expression gives the Gibbs free energy change for the entire water splitting reaction:

$$\Delta G = -nF\Delta E \quad (1.7)$$

At standard temperature (298 K) and concentrations (1 mol/L, 1 bar), a Gibbs free energy change of +237 kJ/mol H_2 translates to the electrochemical cell voltage ΔE of -1.229 V. This indicates that the water-splitting reaction has a thermodynamic advantage. This is in stark contrast to photocatalysis reactions, such as photo-assisted breakdown of organic contaminants, for which the Gibbs free energy change is negative.

1.7. Materials for Semiconducting Photoelectrodes

Important requirements for a semiconductor photoelectrode include efficient visible light absorption and good charge transfer. Usually, but not always, it is simple to establish these parameters from an experiment on a specific material. Clearly, if one wishes to screen an entire class of prospective photoelectrode materials, this method becomes unworkable. In such instances, it may be more fruitful to compute the electronic structure of a base material and utilize this information to forecast how the qualities rely on, for instance, composition. While still far from trivial, calculations of electrical structure are becoming increasingly regular. The necessary computational power and software are widely accessible, and the number of electronic structure calculations reported in the scientific literature, even by experimentally-oriented groups, is rising rapidly. To use these spectra to anticipate certain photoelectrode features, one must first comprehend how the chemical bonding between atoms influences the electrical structure. Several of the fundamental concepts are addressed below. In this thesis, the properties of metal oxide semiconductors are highlighted.

Covalent bonding predominates in the majority of conventional semiconductors such as Si and Ge. For instance, the outer 3s and 3p orbitals of silicon combine to produce hybrid sp^3 orbitals. Neighboring sp^3 orbitals interact to generate bonding and antibonding combinations, which constitute the valence and conduction bands, respectively, of the material.

The nature of the bonding in metal oxide semiconductors is highly distinct. Since oxygen has a significantly higher electronegativity than any metal, the valence electrons are entirely or partially transferred from oxygen to the metal ion. Therefore,

the bonding nature of metal oxides is very polar or even ionic. From the various atomic energy levels, one can construct a molecular orbital (MO) diagram to obtain a qualitative band image. Figure 1.4 is an illustration of rutile TiO_2, the first and most thoroughly studied photoanode material for water splitting (Fujishima & Honda, 1972; Osterloh, 2008). The principal characteristics of the MO diagram correlate pretty well with the estimated band structure of rutile TiO_2. The valence band is dominated by O-2p orbitals, while the conduction band is dominated by Ti-3d orbitals. One may consider the valence band to be filled by the electrons that once dwelt on the titanium atoms but were transferred to the more electronegative oxygen during bond formation.

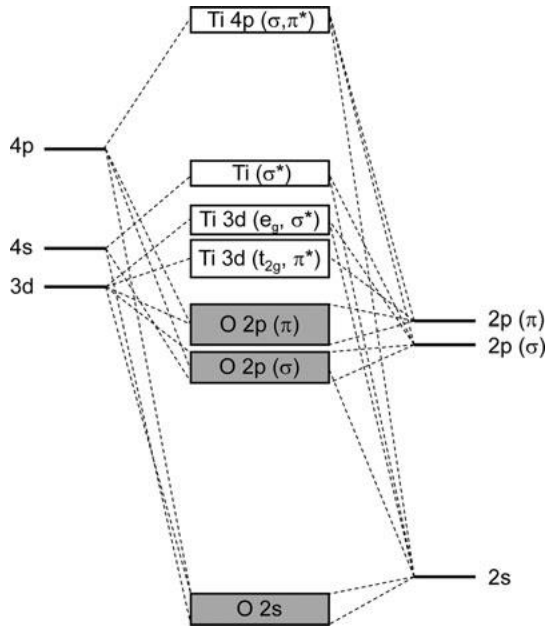

Figure 1. 4. Molecular orbital diagram of rutile TiO_2 (Fischer, 1972; Stoyanov, Langenhorst, & Steinle-Neumann, 2007)

Note that such a "local" perspective is absolutely incorrect for covalent semiconductors such as silicon, in which the electrons are completely delocalized throughout the material. This local versus delocalized perspective is a distinguishing characteristic of metal oxide semiconductors and their covalently bound equivalents. The local nature of the energy bands in metal oxides might lead to misleading readings at times. For instance, sometimes "free" electrons in TiO_2 are differentiated from Ti^{3+} species. While such a distinction is plausible at the surface of a material, where the electronic structure is deformed due to a disturbance in lattice symmetry, it is not evident in the bulk, where the conduction band is predominantly composed of Ti 3d orbitals.

Despite its seeming complexity, the electronic band structure can directly lead to a number of crucial findings regarding photoelectrode materials. The nature of the optical transition is the initial realization. If the highest point of the valence band and the lowest point of the conduction band are placed along the same vector, the optical transition does not need a change in crystal momentum. This type of transition is known as direct. In contrast, transitions that are indirect necessitate a change in crystal momentum. Since photons possess very little momentum, indirect transitions necessitate the absorption or emission of a phonon (i.e., a lattice vibration) and are far less probable. Therefore, the absorption coefficient of indirect semiconductors is two orders of magnitude smaller than that of direct semiconductors Therefore, direct semiconductors, such as amorphous Si or $CuIn_xGa_{1-x}Se_2$ (CIGS), can absorb all incident light in a few micrometers, but crystalline (indirect) Si solar cells are generally 300 mm thick.

Semiconductors used in practical applications are frequently doped, primarily to increase conductivity. Due to the intrinsically poor charge carrier mobilities of metal oxide photoelectrodes, shallow donors and acceptors are nearly always required. The conductivity of the material is given by the equation $\sigma = ne\mu_e + pe\mu_h$, therefore raising n or p will compensate for a small e or h value. Ti^{4+} on a Fe^{3+} site in Fe_2O_3 is an example of a donor-type dopant, as is phosphorus in silicon. The additional valence electron introduced by the donor atom is weakly linked to the donor nucleus and can be stimulated to the conduction band, where it adds to conductivity. In contrast, acceptor-type dopants' holes can be stimulated to the valence band. Since a hole corresponds to a missing electron, this can also be visualized as an electron being stimulated from the valence band to the energy level of the acceptor species.

1.8. Defect Chemistry

Almost always, semiconducting photoelectrodes are doped to increase their characteristics. In the majority of instances, the objective is to boost the n- or p-type conductivity, as detailed in Section 1.6. Certain dopants can improve the optical absorbance of wide bandgap semiconductors (Sato, 2002), the minority carrier diffusion length (Maruska & Ghosh, 1979; Salvador, 1982), or the surface catalytic activity of the semiconductor (Hervieu, 1995). By introducing midgap bulk or surface states that

operate as recombination centers, for instance, other dopants have a negative effect on the characteristics (Kato & Kudo, 2002).

In addition to foreign cation and anion dopants, the material typically has native point defects. Examples are voids, interstitials, or substituents. These flaws can affect the optical, electrical, and catalytic properties similarly to dopants. They are generated by intrinsic defect-chemical processes or by a change in the lattice stoichiometry resulting from the exchange of, for instance, oxygen with the gas phase. For constructing effective photoelectrodes, it is of the utmost significance to comprehend and forecast the interaction between dopants and defect concentrations, as almost every defect influences the performance of the material in some manner.

1.8.1. Doping Bimetallic Oxides

Due to the similarity of the lattice sites of covalently bound semiconductors, the incorporation of dopants is quite simple. This is true even for polar compounds like GaAs. Si can be inserted on both Ga and As lattice sites in this material (Piazza, Pavesi, Henini, & Johnston, 1992). The situation is much different for ionically coupled materials, as the huge electrostatic penalty inhibits any exchange of anions and cations. This imposes the following limits on the inclusion of dopants.

The Kroger–Vink notation can be used to succinctly explain the incorporation of dopants in metal oxides and other ionic materials (Schmalzried, 1964). As with any other chemical (half)reaction, the conservation of mass and charge must be observed while defining defect-chemical processes. The conservation of lattice site stoichiometry is what distinguishes the defect chemistry of ionic solids. When Fe_2O3 is doped with zinc oxide, for instance, two zinc ions replace Fe and two oxygen ions occupy two of the three oxygen sites in the Fe_2O_3 unit. This results in an oxygen vacancy, as the third oxygen spot stays unoccupied.

1.9. Thesis Overview

The main objective of this Ph.D. thesis was to develop a novel semiconductor electrode material for electrochemical water splitting.

The details of each chapter were described below:

i. In Chapter 2, the photoelectrochemical measurement methods will be described in detail. Specific characteristics of a photoelectrochemical cell will be mentioned and also design of the cell will be told in detail. After, for an electrochemical measurement which substrates can be used, and the qualities of an electrode substrates will be mentioned. In addition, details for an electrode material will be discussed. Furthermore, specific characteristics for a counter and reference electrode will be discussed. Also, which electolytes can be used as electrolytes will be mentioned. Lastly, we will discuss our own cell design, samples, substrates, counter and reference electrodes and electrolytes.

ii. In Chapter 3, we will discuss the combinatorial identification and optimization of new oxide semiconductors. We will talk about recent literature studies. We will explain the inkjet printer modes, the features of the inks used and the printer conditions in detail. We'll talk about catalyst-based ink development later. prerequisites, carrier solvents, functional types and precursors will be explained in detail. Then, catalyst-based solutions will be mentioned. Additive materials to be used in inks will be discussed. The latest nickel-based multi-metal oxides will be discussed. In the last part of the chapter, the characterization and electrochemical properties of the ink and nickel-based catalysts we have developed will be discussed.

iii. In chapter 4, perovskite materials containing Ba will be mentioned. BSCF, which is a promising perovskite materials according to recent literature studies, will be mentioned and how the results change with silver doping to BSCF will be discussed. In addition, detailed information about why silver is added will be shared. General information about perovskite oxide catalysts will be shared. Finally, the electrochemical and morphological differences between BSCF and BSCF-Ag will be discussed.

CHAPTER 2

PHOTOELECTROCHEMICAL MEASUREMENTS

2.1. Introduction

Despite the many advances in computational materials science in the last decade, photoelectrochemical water splitting is still very much an experimental field. This is because many of the relevant properties of photoelectrodes are determined by factors that are either difficult to control or not yet well understood, which makes it difficult to predict a priori their influence on the actual performance. An example of this is the presence of certain defects, such as dislocations or impurities. These are often impossible to avoid, especially when low-temperature and low-cost synthesis methods are used. An important stage in the development process of a photoelectrode is therefore to systematically optimize the synthesis procedure to achieve a maximum photoresponse.

A common metric to determine the optimal photoresponse is the photocurrent density under 1 sun illumination (1,000 W/m^2). To be able to compare the photocurrent for different samples, two criteria should be fulfilled. The main one is that the measured data reflect the properties of the sample, as opposed to artifacts or limitations caused by the measurement setup. For example, mass transport limitations should be avoided by careful design of the electrochemical cell, and Ohmic losses and pH fluctuations can be avoided by choosing a suitable electrolyte. For a meaningful comparison of performance numbers reported by different laboratories one should also fulfill the second criterion, which is that the measurements must be performed under the exact same conditions. While seemingly trivial, there are many performance claims in the literature that fail to meet this requirement. This can be due to lack of, e.g., proper equipment (calibrated light sources in particular), but also to missing information in the paper to which the authors compare their results. To avoid this, one should be careful to mention at least the sample area and thickness, the intensity and type of light source used, the electrolyte composition and pH, the cell geometry and counter electrode area, and the applied potential.

In addition to performance evaluations, many photoelectrochemical experiments are aimed to identify performance-limiting steps or to determine certain materials properties. Examples of the latter are donor or acceptor densities and the flatband potential of a material, which can be determined by electrochemical impedance measurements. The challenge with these measurements is that they always yield data, but that it can be difficult – and sometimes even impossible – to translate the measured data to the desired materials parameters. Carefully performed control experiments and a good basic understanding of the measurement equipment – in particular, the potentiostat and the frequency response analyzer (FRA) – are essential for obtaining meaningful results.

Much information on photoelectrochemical measurements and measurement equipment is available, but it is often scattered throughout the various papers, books, and technical notes of manufacturers. Moreover, many practical methods and tricks are passed on by communication between colleagues or between supervisors and students and cannot be found in the literature. This chapter attempts to bring some of the basic information on photoelectrochemical measurement techniques and equipment together and aims to serve as a quick start for students and other newcomers in this exciting field.

2.2. The Photoelectrochemical Cell

One of the key components of a photoelectrochemical setup is the photoelectrochemical cell (further abbreviated as PEC cell) in which the photoanode or photocathode is mounted. At bare minimum, a PEC cell consists of a reservoir to hold the electrolyte, the sample to be studied (the working electrode), a counter electrode to supply current, an optically transparent window that allows the sample to be illuminated, and facilities to electrically connect both electrodes to the outside world. Other components that are often present are a reference electrode, a quasireference electrode (see Sects. 3.2.4 and 3.6.6), and one or more inputs and outputs for a gas circulation system and/or gas purging of the electrolyte. In addition, one may encounter a magnetic stir bar, and a membrane that separates the anode and cathode compartments to avoid mixing of the evolved oxygen and hydrogen gases.

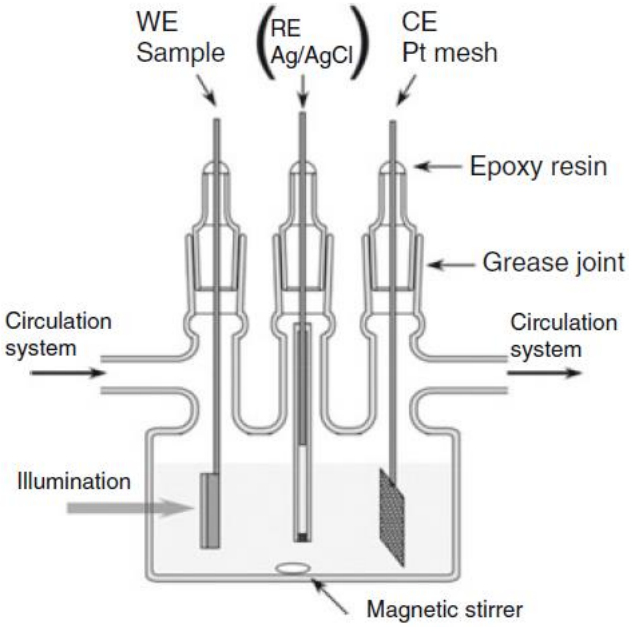

Figure 2. 1. Example of a conventional photoelectrochemical cell

2.2.1. Cell Designs

An example of a common PEC cell design is shown in Fig. 2.1. This design is based on that of conventional electrochemical cells used for, e.g., corrosion studies. The main aspect that distinguishes the PEC cell from a standard electrochemical cell is the presence of an optically transparent window through which the sample can be illuminated. Since normal glass shows a transmission cut-off below ~350 nm, fused silica (amorphous SiO_2) is most often used as a window material in PEC cells. UV-grade fused silica is transparent in the entire range from UV to near-IR with a transmission >90% between 200 nm and 2.2 mm. It shows excellent chemical stability in both acidic and alkaline aqueous solutions (except in HF) and is relatively cheap. Cells such as the one shown in Fig. 2.1 are commercially available, robust (despite being constructed entirely from glass), and easy to use when it comes to mounting the electrodes. There are also some disadvantages. As it is made from glass, the cell can be rather large and may require a large amount of electrolyte (>100 mL). This quickly becomes impractical when screening large numbers of photoelectrodes. Moreover, the distance between the working and counter electrodes usually exceeds 5 cm and may give rise to Ohmic voltage losses at higher current densities (see Sect. 3.2.5). A more

practical issue is sample mounting: since the sample is fully immersed in the electrolyte, it needs to be partially masked with, e.g., epoxy resin to avoid any direct contact between the electrolyte and the conducting back-contact and/or the connecting wire.

To address these issues, many groups design their own photoelectrochemical cells that are specifically optimized for the types of samples and experiments that are carried out in their laboratories. Figure 2.2 shows an example of a cell that was developed by the author's laboratory. It has a modest volume (~30 mL), and the sample is mounted in a detachable sample insert for ease of handling. The sample insert is pressed against an O-ring seal on the cell body via ring that is threaded at the outside (R_1). A similar ring (R_3) is used to mount the fused silica window at the front of the cell. The sample surface is pressed against an O-ring with another threaded insert (R_2). Electrical contact to the sample is made with a thin copper wire that is glued to the sample with carbon or silver paste. The wire is guided to the outside via a narrow slot (F) in the sample insert. The design ensures that the sample area wetted by the electrolyte is the same as the illuminated area. The sample can be illuminated from the front or from the back. Since the center of the sample coincides with the center of the four alignment rods, switching from front- to back-illumination can be done by rotating the cell 180° without risk of losing optical alignment. At the bottom of the cell a cylindrical hole is made to accommodate a small magnetic stirbar, and the same hole is connected to a drain at the front of the cell. The drain allows the electrolyte to be refreshed without removing the cell or the cell lid from the setup. The feedthroughs in the lid of the cell are threaded on the inside, with an O-ring seal to ensure gas tightness.

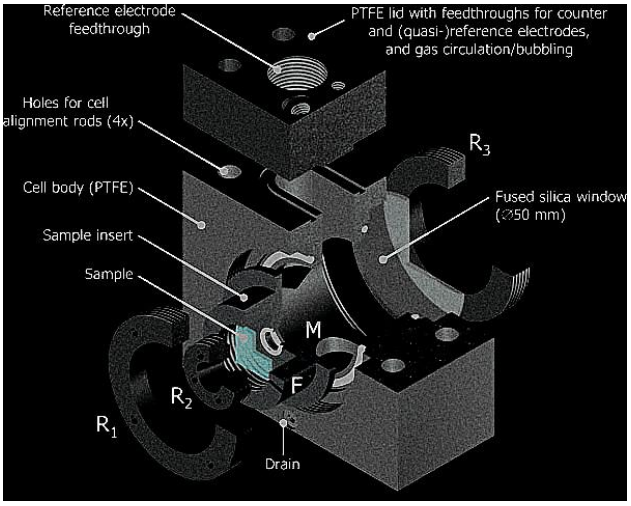

Figure 2. 2. Photoelectrochemical cell used by our group

2.2.2. Sample and Substrate

From a practical point of view, the main characteristic of a photoanode or photocathode sample is whether the film is compact or porous. Compact films can be easily sealed by gently pressing them against an O-ring. The area that is exposed to the electrolyte can be accurately determined, which is essential for, e.g., donor density calculations using the Mott–Schottky relationship. Moreover, the illuminated area is the same as the wetted area, which minimizes dark current contributions to the total current. Porous films can be mounted by gluing them to a mask with a hole that defines the area to be wetted. The choice of glue or sealant is critical: it needs to be chemically resistant in the electrolyte to be used, and it also needs to have a high viscosity to prevent the infiltration of the porous film in the area that is exposed to the electrolyte. In practice, this limits the choice to certain epoxy resins, or to certain thermoplastic polymers that soften between ~100 and 200 °C. Examples of the latter are Surlyn® and Bynel® from Dupont, which are used to seal dye-sensitized solar cells based on mesoporous TiO_2. These sealants are sold as 25–50 mm sheets and are convenient to use, but somewhat costly. Alternatively, one can simply immerse the entire sample (except the top part) in the electrolyte. Care should be taken that the entire sample is coated to avoid direct exposure of the conducting substrate to the electrolyte. This is the most convenient method for photocurrent measurements on porous films. However, it is not suited for quantitative impedance analysis, since the meniscus at the sample/water/air interface results in a poorly defined sample area.

Photoelectrochemical measurements on thin film samples require a conducting substrate as a back-contact. Optically transparent substrates are usually preferred since this also allows the sample to be illuminated from the back. The substrate should form an Ohmic contact with the photoactive material to ensure uninhibited current flow. For n-type photoanodes, this requires conducting materials with a work function that is lower than that of the photoanode itself. In most cases, transparent conducting oxides (TCOs) are used. These materials have high carrier concentrations and mobilities, but still show good optical transparency (>80%) because their plasma frequencies are in the near infrared ($\lambda p > 1$ mm). They are deposited as a 100–400 nm film on glass by sputtering or spray pyrolysis. Examples of TCOs are F-doped SnO_2 (FTO), Sb-doped SnO_2 (ATO), Sn-doped In_2O_3 (ITO), and Al-doped ZnO (AZO). Table 2.1 indicates several key materials properties of important TCOs. Many other TCOs exist, but FTO

and ITO are most common ones that are commercially available. Examples of suppliers are Pilkington, Asahi, Libbey–Owens–Ford, and several smaller ones such as Solaronix and Dyesol. Typical sheet resistances of commercial TCOs on glass are 8–30 Ω/sq. ITO has a ~2 times higher conductivity than FTO, but shows poorer thermal stability and chemical resistivity (Gordon, 2000). Since sheet resistances are not (yet!) limiting the performance of PEC cells for water splitting, FTO is currently the conducting substrate of choice. For p-type photocathodes, high-work function back-contacts such as gold and platinum can be used. It should be noted that work function differences do not always correctly predict the formation of an Ohmic or Schottky contact. For example, FTO appears to form an Ohmic contact with certain p-type materials such as Cu_2O (de Jongh, Vanmaekelbergh, & Kelly, 2000).

Table 2. 1. Typical materials parameters for some common TCOs (Ferekides, Mamazza, Balasubramanian, & Morel, 2005; Fortunato, Ginley, Hosono, & Paine, 2007; Gordon, 2000; Minami, 2000; Minami, Miyata, & Yamamoto, 1999)

TCO Material	**Highest Conductivity (S/cm)**	**Carrier Concentration (cm^{-3})**	**Mobility ($cm^2/V's$)**	**Work Function (eV)**	**Thermal Stability in air (°C)**
In_2O_3:Sn (ITO)	~1 X 10^4	~10^{21}	~40	4.7	<350 °C
SnO_2:F (FTO)	~1 X 10^3	4 X 10^{20}	~30	4.9	<700 °C
ZnO:Al (AZO)	~7 X 10^3	1.5 X 10^{21}	50-100	4.6	<400 °C

The choice of conducting substrate becomes more difficult when postdeposition high-temperature treatments are necessary. This is often the case for complex oxides, such as perovskites or oxynitrides (Abe, Higashi, & Domen, 2010), which may require firing at temperatures above 600 °C in order to obtain the desired crystalline phase. This prohibits the use of float glass, which softens above ~550 °C. Certain types of borosilicate glass can be used up to 650 °C, while fused silica or sapphire can withstand continuous exposure to temperatures up to 950 °C. Unfortunately, the conductivity of ITO films quickly decreases above 350 °C. FTO and ITO/FTO coatings are stable up to

600–700 °C (Gordon, 2000; Goto, Kawashima, & Tanabe, 2006), and may still have acceptable conductivities at higher temperatures provided the anneal treatment is kept sufficiently short (<30 min). For higher temperatures and/or longer times one needs to switch to thin noble metal films (e.g., Pt), at the price of significantly poorer optical transmission properties.

2.2.3. The Counter Electrode

To avoid performance limitations, the reaction at the counter electrode should be fast and the electrode itself should have a high catalytic activity. A common materials choice is Pt, which combines good chemical stability with a very small overpotential for hydrogen evolution (~0.1 V). Ideally, the surface area should be at least two times larger than the working electrode area, and both electrodes should face each other symmetrically to avoid inhomogeneous current densities at the working electrode. For high electrolyte concentrations (typically >0.5 M, see below), the latter requirement is less stringent due to the modest voltage drop across the electrolyte solution. A common configuration is a coiled Pt wire electrode or a piece of Pt wire mesh at about ~1 cm in front of the working electrode. A circular hole in the mesh is necessary to avoid it from blocking the light. A piece of TCO glass coated with a sputtered film of Pt is a low cost and – in most cases – perfectly acceptable alternative.

2.2.4. The Reference Electrode

When studying the properties of the working electrode – either a photoanode or a photocathode – the applied potential is a key parameter. This potential should be measured with respect to a fixed reference potential, so that any change in the applied potential reflects a change in the working electrode alone. The counter electrode cannot be used for this, since the overpotential at the counter electrode/ electrolyte interface is generally unknown and varies with the amount of current flowing through the cell. To avoid this current-dependence, a third electrode is added to the electrochemical cell: this is the reference electrode. The potential of the working electrode can now be measured with respect to the (fixed) potential of the reference electrode with negligible current flow through the latter.

Table 2.2 shows an overview of commonly used reference electrodes in solar water splitting research. Applied potentials are nowadays usually reported against the RHE scale for water splitting studies. Zero volt on the RHE scale reflects the H^+/H_2 redox potential in the actual solution, irrespective of the pH. This makes it more convenient to use than the NHE scale, for which $\Phi(H^+/H_2) = 0$ V only at unit activity of the H^+ ions and the dissolved H_2 gas. Silver/silver chloride electrodes are most commonly used as reference electrodes, and have largely replaced the traditional and environmentally less friendly saturated calomel electrodes (SCEs) that are based on Hg/Hg_2Cl_2. A potential measured with respect to Ag/AgCl ($\Phi_{Ag/AgCl}$) can be converted to the RHE scale (Φ_{RHE}) with the following expression:

$$\Phi_{RHE} = \Phi_{Ag/AgCl} + \Phi^0_{Ag/AgCl\ vs.SHE} + 0.059 \times pH \quad (2.1)$$

Table 2. 2. Overview of reference electrodes commonly used in PEC research (Compton & Banks, 2007)

Reference electrode	**Filling solution**	**Potential (vs. SHE)**	**Remarks**
Reversible hydrogen	Actual electrolyte solution, purged with H_2 gas	0.0 – 0.059 X pH	RHE: This is nowadays the preferred reference scale for publications on solar water splitting.
Standard hydrogen (= normal hydrogen)	$[H^+]$ = 1.18 mol/L, $p(H_2) = 10^5$ Pa	0.000	SHE (=NHE): Often used as reference in the literature, but now being replaced in favor of the more convenient RHE scale.
Silver/silver chloride (Ag/AgCl)	0.1 M KCl 1 M KCl 3 M KCl 3.5 M KCl Saturated KCl	0.289 0.237 0.210 0.205 0.198	Workhorse for PEC research

Cont. on the next page

Cont. of Table 2.2

Calomel (Hg/Hg_2Cl_2)	3 M NaCl	0.209	NCE
	Saturated NaCl	0.197	
	1 M KCl	0.334	
	3 M KCl	0.281	
	3.5 M KCl	0.250	
	Saturated KCl	0.242	SCE
	Saturated NaCl	0.236	SSCE

Here, $\Phi^0_{Ag/AgCl\ vs.SHE}$ is the potential of the Ag/AgCl reference electrode with respect to the standard hydrogen potential (SHE). To give an example, a potential of 0.23 V vs. Ag/AgCl (satd.) in a 1 M KOH solution of pH 13.6 corresponds to a potential of 1.23 V vs. RHE.

2.2.5. The Electrolyte

The electrolyte in an electrochemical cell consists of a solvent in which the active species to be reduced or oxidized are dissolved. For photoelectrochemical water splitting, the solvent and the active species are one and the same: water. However, since pure water is poorly conducting, supporting ions must be added to ensure that the desired current flow can be attained. The concentration of the supporting electrolyte should be sufficiently high to avoid large Ohmic voltage losses across the electrolyte. These Ohmic losses must be compensated by increasing the applied bias potential, which adversely affects the overall efficiency of the photoelectrode. The voltage drop is given by $V_{loss} = I\ X\ R_E$, where I is the total current flowing between the working and counter electrodes, and R_E is the electrolyte resistance. The latter is determined by the conductivity of the electrolyte, k, and the cell constant, K_{cell}, according to:

$$R_E = \frac{K_{cell}}{k} \tag{2.2}$$

The cell constant depends on the geometry of the cell, and can be determined from an ac impedance measurement of RE using a standard electrolyte solution of known conductivity.

The electrolyte conductivity depends strongly on the type of dissolved ions and their concentrations. It is important to realize that the relationship between the conductivity and the concentration is in general non-linear. This is due to either incomplete dissociation of the anions and cations (in the case of so-called weak electrolytes) and/or ion–solvent interactions. Deviations from linearity may already occur at concentrations above 1 mmol/L and will certainly play a role in practical water splitting applications. At very high concentrations (>1M), ion-pair formation may result in a decrease of the conductivity with concentration. Therefore, an aqueous solution of KOH shows a conductivity maximum at a concentration of ~6 M. Table 2.3 gives an overview of the conductivities of several electrolyte solutions often used in PEC studies. To give a rough idea of the Ohmic losses that can be expected, Table 2.3 also includes the voltage drop across the electrolyte for a current density of 5 mA/cm^2. Clearly, concentrations of at least 0.5 M are required to keep Ohmic losses at an acceptable level. Moreover, potassium-based salts are preferred over sodium salts from a conductivity point of view.

In practice, aqueous H_2SO_4 or HCl solutions (0.5–1 M) are often used as an acidic electrolyte for, e.g., WO_3 (Santato, Odziemkowski, Ulmann, & Augustynski, 2001) or TiO_2. For WO_3, NaCl has also been used to simulate saline conditions (Alexander, Kulesza, Rutkowska, Solarska, & Augustynski, 2008). For photoelectrodes that require neutral or alkaline solutions, such as a-Fe_2O_3 (Kay, Cesar, & Grätzel, 2006), 0.5–1 M KOH or NaOH solutions are commonly used. Some metal oxides are only stable in neutral environments. An example is $BiVO_4$, which is only stable between pH 3 and 11 and is usually studied in an aqueous solution of 0.5 M Na_2SO_4 or K_2SO_4 (Sayama et al., 2006). To avoid local pH fluctuations in this solution – which would affect the flatband potential – one should consider adding a pH buffer to the solution. A suitable choice is the well-known phosphate buffer KH_2PO_4/K_2HPO_4, which gives a pH of 6.86 at 25 °C when adding 0.025 M of each species to the electrolyte.

To efficiently remove the evolved hydrogen and oxygen from the electrolyte solution, the electrolyte should be continuously purged with an inert gas such as nitrogen or argon. This prevents the back-reaction of dissolved H_2 and O_2 to water and ensures that the redox potentials do not change over time (both H_2 and O_2 appear in the Nernst equations for water reduction and oxidation). Continuous purging through the electrolyte solution must be avoided when the generated bubbles interfere with the light path and generate excessive noise on the photocurrent signal. If this is unavoidable, one

can purge the solution thoroughly (at least 20 min) before starting the experiment and hang the purge tube above the electrolyte to generate a blanket of inert gas above it. Stirring the solution with a magnetic stir bar greatly enhances the purging efficiency and ensures quick removal of any dissolved oxygen. Stirring to address mass transport limitations in the electrolyte is usually not necessary in view of the high ionic concentrations and is often avoided to prevent measurement noise.

Table 2. 3. Electrical conductivities for various electrolytes and the corresponding electrolyte resistances and voltage drops for a current density of 5 mA/cm^2 (Gilliam, Graydon, Kirk, & Thorpe, 2007)

Reference electrode	***k* (Ω^{-1} m^{-1})**	***R*$_E$ (Ω)**	***V*$_{loss}$ @ 5 mA/cm^2 (mV)**	**T (°C)**	**Ionic species (in H_2O)**	**Limiting ionic conductivity (10^{-4} Ω^{-1} mol^{-1} m^2)**
1.0 M KOH	20.1	5.0	25	20	H^+	349.8
0.5 M KOH	10.7	9.3	47	18	K^+	73.5
0.1 M KOH	2.26	44	221	18	Na^+	50.1
0.5 M NaOH	8.6	12	58	18	OH^-	197
Satd. NaCl (~5 M)	21.4	4.7	23	18	Cl^-	76.4
1.0 M NaCl	7.44	13	67	18	SO_4^{2-}	162
0.5 M NaCl	3.8	26	132	18		
0.1 M NaCl	1.07	93	467	18		
3.5 M H_2SO_4	73.9	1.4	7	18		
1.0 M H_2SO_4	36.6	2.7	14	18		
0.5 M K_2SO_4	6.2	16	81	20		
Distilled water	10^{-3} to 10^{-4}	10^5 to 10^8	∞	20		
Millipore water	~5.5 X 10^{-6}	~18 X 10^6	∞	25		

CHAPTER 3

COMBINATORIAL IDENTIFICATION AND OPTIMIZATION OF NEW OXIDE SEMICONDUCTORS

3.1. Introduction

Heterogeneous catalysis plays a key role in the production of about 90% of chemicals worldwide (Maleki & Bertola, 2020). Because of its significant impact, researchers in chemical and energy areas, have invested much effort in the development of this field (Ross, 2012). In heterogeneous catalysis, reactions usually occur at the solid catalyst-fluid interface, and the activity depends on the interactions of reactants and the catalyst surface. Thus, the catalyst surface morphology is as important as the surface chemical composition (Maleki & Bertola, 2020). A great variety of reactors have been developed to immobilize solid catalysts efficiently for catalytic reactions, such as conventional fixed-bed and fluidized-bed reactors or, more recently, using monolithic reactors, membrane reactors and microreactors (Maleki & Bertola, 2020). For example, in microreactors, higher surface-to-volume ratio due to small length-scale would lead to heat and mass transfer enhancement. Therefore, this type of reactor is utilized for various reaction types and in-depth kinetic studies (Kolb & Hessel, 2004; Wörz, Jäckel, Richter, & Wolf, 2001).

In heterogeneous catalysis, the solid catalyst is normally deposited onto the reactor channel walls for various reaction conditions. Different deposition techniques have been integrated into reactor and microreactor technologies for efficient and uniform catalyst immobilization (Mehla et al., 2019; Meille, 2006). Dip-coating is often used for the layered deposition of catalyst by immersion and withdrawal of the substrate into the catalyst-based solution (Balzarotti et al., 2022). This method can be used for coating of packed-bed pellets or monolithic reactors which are widely used as automotive catalytic converters (Maleki & Bertola, 2020). Doctor blade and spin-coating are generally used for the coating of flat substrates (Berni, Mennig, & Schmidt, 2004; Kontos, Kontos, Tsoukleris, Vlachos, & Falaras, 2007). Despite the fast

processing and ease of operation, these methods produce large waste of materials (Bharathan & Yang, 1998). Furthermore, they are not suitable for patterned deposition and for producing ultra-thin films (Morozova et al., 2011). Vacuum deposition refers to a class of deposition methods used to coat materials atom-by-atom or molecule-by-molecule onto the substrate (Maleki & Bertola, 2020). Vacuum deposition methods are operated under low pressures (i.e., vacuum) and can create ultra-thin films (Mattox, 2010). Physical and chemical vapour deposition methods have been recently used for catalyst deposition (J. Lu, Elam, & Stair, 2016; Maric, 2008; Won et al., 2011). Despite the potential advantages provided by vacuum deposition methods, such as monitoring of film thickness and purity, they involve expensive multi-step operations at elevated temperatures (Raut & Al-Shamery, 2018).

Inkjet printing is a fast-growing technology for deposition of functional materials on various substrates in electronics (Aleeva & Pignataro, 2014; Raut & Al-Shamery, 2018), pharmaceutical (Scoutaris, Alexander, Gellert, & Roberts, 2011; Singh, Haverinen, Dhagat, & Jabbour, 2010) and micro-engineering industries (Maleki & Bertola, 2020). Inkjet printing is a non-contact deposition method which takes an image or pattern data from a computer and applies it onto a substrate using ink in the form of microdroplets (Mohebi & Evans, 2002). This method has a high-precision control over homogenous deposition of picolitre-sized droplets and can be operated at ambient temperature and pressure (Maleki & Bertola, 2020). Moreover, complex patterns can be easily produced by using inkjet printing without the use of physical masks (ZhouPing Yin, Huang, Bu, Wang, & Xiong, 2010). Therefore, it offers cost-effective rapid mass production of various materials from thermosensitive substances (de Gans, Duineveld, & Schubert, 2004) to metal oxides (Turner, Aspinall, Rushworth, & Black, 2019) with minimal waste of materials. Table 3.1 presents a summary of different deposition techniques in comparison to inkjet printing.

Due to the advantages of inkjet printing and the large number of applications, many research groups are active in developing this technique in different fields of technology. Moreover, several review articles have been published focusing on different aspects of the technology such as: (i) inkjet printing of metal oxide-based precursors (X. Liu, Tarn, Huang, & Fan, 2015; Perelaer et al., 2010), (ii) ink formulation of metal nanoparticles and metal–organic compounds for printed electronics (Maleki & Bertola, 2020), (iii) development of printing technologies and sintering approaches for fabrication of flexible electronics (Raut & Al-Shamery, 2018;

Wünscher, Abbel, Perelaer, & Schubert, 2014), (vi) ink drop impact and interaction with the substrate (Maleki & Bertola, 2020) etc.

Table 3. 1. Comparison of typical deposition technologies

	Spin/dip-coating	**Lithography**	**Vapour deposition**	**Inkjet printing**
Material waste	High	High	Low	Low
Working Area	Medium	Small	Small	Large
Patterning capability	Low	Medium	Low	High
Temperature	Low	High	High	Low
Mask required	Yes	Yes	Yes	No
Process	Simple	Multi-step	Multi-step	Simple
Cost	Low	High	High	Low

3.2. Inkjet Printing: Methodology

The first modern movable printing press was developed by J. Gutenberg in the 15th century (Maleki & Bertola, 2020). In this printing machine and later conventional derivatives such as offset printing and screen printing, the pressure is applied on the substrate during the ink transfer, which is known as contact-printing (Vollmann, 1980). In recent printing technologies, ink is transferred to the substrate without applying physical contact between the ink dispenser and the substrate, which is referred to as noncontact-printing (Maleki & Bertola, 2020). In non-contact printing, the substrate is only in contact with the ink containing the printing material, and there is no mechanical pressure on the substrate, which removes the risks of damaging the pre-patterned substrate or of causing contamination. Furthermore, non-contact printing allows for patterned printing and multilayered deposition with high accuracy, resolution and speed (Raut & Al-Shamery, 2018).

Inkjet printing as a non-contact method emerged for direct patterned deposition of solution-based materials. In this method, ink is delivered to the nozzle-head from the

ink reservoir and ejected in the form of microdroplets. The released ink droplets hit the substrate at specific rates to perform the printing (Singh et al., 2010). The printed patterns can be created by controlled displacement of either the substrate or the print-head. Then, the printed ink goes through the evaporation and solidification process. Usually, the printed substrate is post-processed at high temperatures in form of thermal annealing, sintering or calcination to remove solvents, increase the adhesion and modify the material structure (Hon, Li, & Hutchings, 2008).

3.2.1. Inkjet Printing Modes

Inkjet printers have two main operational modes: continuous and drop-on-demand (DOD). In continuous inkjet printing, the ink fluid is released from the nozzle in the form of a liquid jet. The liquid jet undergoes the surface tension-driven jet break-up, which is known as Plateau–Rayleigh instability, and breaks up into droplets (Hon et al., 2008). Continuous inkjet printing is normally used in textile printing and labelling due to highspeed operation (de Gans et al., 2004). Drop-on-demand (DOD) inkjet printing is the method of choice, in most cases, alongside the continuous mode due to higher precision and smaller drop size and flexibility of ink formulations (Maleki & Bertola, 2019).

In DOD mode, two types of actuators are widely used: piezoelectric actuators and thermal actuators (Sirringhaus & Shimoda, 2003). In piezoelectric DOD printing, ink droplets are formed and released by deformation of the piezoelectric actuator induced by an electric field (H. Jiang & Tan, 2018). By applying a certain electric potential to the piezoelectric transducer, a pressure wave is created due to a small volume change. The pressure wave moves towards the nozzle and drives out the ink droplet as shown in Fig. 3.1. In a thermal drop-on-demand inkjet printer, the ink solution is heated using a Joule heating element placed ear the nozzle. A bubble of ink vapour is formed, which routs out an ink microdroplet. In other words, the thermal DOD process uses the evaporation of a tiny volume of ink to create the ink droplet and jetting driving force (de Gans et al., 2004). Therefore, the ink selected for this method should have volatile components such as water or short-chain alcohols. On the other hand, piezoelectric DOD printing is suitable for a wide variety of ink solvents since the ink drop formation and release are based on the ink volume change caused by the

fluctuation of the piezoelectric membrane. Furthermore, the rate and size of jetted droplets can be adjusted precisely by regulating the working voltage without the need for temperature alteration (de Gans et al., 2004; Raut & Al-Shamery, 2018).

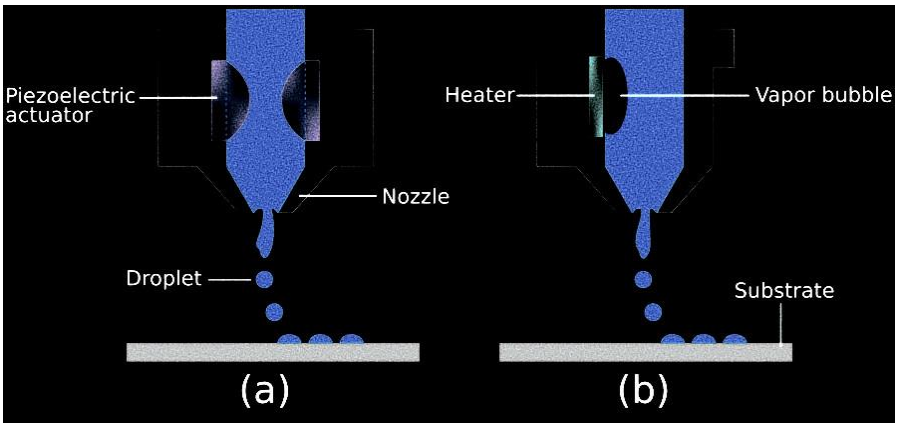

Figure 3. 1. Schematic illustration of drop-on-demand inkjet printing process: (a) piezoelectric DOD mode and (b) thermal DOD mode.

3.2.2. Ink Properties and Printing Conditions

In the inkjet printing technology, the ink solution should be carefully formulated to have specific properties such as particle size distribution, density, surface tension and viscosity (H. Jiang & Tan, 2018). In addition to the ink characterization, the printing condition needs to be regulated to yield stable droplets. In other words, ink solutions should be prepared for a particular printing condition both in terms of stability, and in terms of rheological and interfacial properties. Nanoparticles dispersed in the ink solutions tend to form secondary micron-sized agglomerates leading to particle sedimentation. Moreover, rapid evaporation of the solvent at the nozzle and large particle agglomerates may cause nozzle clogging (Addamo et al., 2004). Therefore, it is preferable to stabilize the inkjet solution using dispersing agents and use particles with average size as small as 1/50th of the nozzle diameter (Maleki & Bertola, 2019; Sundriyal & Bhattacharya, 2017). The ink viscosity and surface tension also strongly influence the dynamics of microfluidic droplets and must be carefully controlled and/or optimized. The suggested range for viscosity in DOD inkjet printers is 1–25 mPa s (Cummins & Desmulliez, 2012). Ink solutions with higher viscosity cannot release smoothly from the nozzle. At the same time, low viscous inks form unstable droplets during the printing process resulting in the formation of satellite micro drops. The

suggested surface tension range in DOD mode is 20–50 mN m^{-1} (Maleki & Bertola, 2020). Higher surface tensions hinder the drop formation process and lower surface tensions would lead to air ingestion and dripping of droplets towards the substrate (Waasdorp, van den Heuvel, Versluis, Hajee, & Ghatkesar, 2018).

Although surface tension and viscosity are the main physical properties that determine the drop formation and size, the jetting capability of the formulated ink also depends on the nozzle size and the printing conditions. These parametric quantities are merged into the Reynolds number and the Weber number, representing the ink fluidic properties (Mahbubul, Saidur, & Amalina, 2012):

$$R_E = \frac{\rho v d}{\eta} \tag{3.1}$$

$$W_E = \frac{\rho v^2 d}{\gamma} \tag{3.2}$$

Here, γ, ρ and η are the surface tension, density and dynamic viscosity of the fluid, respectively, d is the nozzle size, and v is the fluid drop velocity. These dimensionless values are usually combined into a single parameter, the inverse Ohnesorge number:

$$Z = O_h^{-1} = \frac{R_e}{\sqrt{W_e}} = \frac{\sqrt{\rho \gamma d}}{\eta} \tag{3.3}$$

which is often used to describe the inkjet printing condition. As given in eqn (3.3), the Ohnesorge number does not depend on the fluid velocity, v, therefore O_h^{-1} only accounts for the physical properties of the fluid and the characteristic length (Maleki & Bertola, 2020). According to the literature, ink droplets are printable in a DOD inkjet printer when $1 < Z < 10$ (Reis & Derby, 2000). In the high viscous region ($Z < 1$), the fluid cannot turn into droplets, and in the low viscous region, inkjet printing would result into the generation of satellite droplets ($Z > 10$) (Derby, 2010). However, the parameter O_h^{-1} gives only an approximate quantification of the ink printability. It was reported that (Maleki & Bertola, 2020) reported that splashing occurs when the droplet falls onto a surface at a speed above a critical limit, or $W_e^{1/2} R_e^{1/4} > 50$. It was suggested (Maleki & Bertola, 2020) a minimum value for Weber number, $W_e = 4$, above which there is enough kinetic energy in the ink flow to overcome the surface tension and form

smaller diameter droplets. These limiting thresholds attempt to define regions where drop formation and DOD inkjet printing are achievable. Furthermore, they can predict the printability of the newly formulated inks. There exist comprehensive textbooks and reviews to understand the fundamentals of inkjet ink preparation which would be helpful for further studies (Derby, 2010).

3.3. Catalyst-Based Ink Development

Ink formulation is a key step in the inkjet printing technology since the prepared ink should maintain specific properties to meet the printing requirements. The inkjet inks for DOD mode usually contain functional species precursor, carrier solvent and additives. The precursor for catalyst-based inks is composed of metal oxide particles, metal salts or metal-based solutions. To date, there are limited reports on the ink development of inorganic materials due to preparation and storage challenges. This section will summarize the ink formulation requirements and specific approaches to use various components for catalyst-based ink preparation.

3.3.1. Prerequisites

While the basic principles of inkjet printing are rather simple, the printer components such as the printhead and nozzles are complex structures which can operate reliably only with ink fluids with specific properties (Maleki & Bertola, 2020). Therefore, some points need to be addressed in the design of catalyst-based inks:

i) The ink formulation should be compatible with the printer components. For example, the carrier solvent should not damage the nozzles and the ink delivery system.

ii) The ink should have viscosity and surface tension within specific ranges to operate in the inkjet printer, and these properties may differ in different printing systems.

iii) Stability is key in designing inks since the agglomeration of ink components would cause nozzle clogging and blockage of ink delivery system thereby limiting the ink lifetime.

iv) The prepared ink should have effective adhesion to the substrate with sufficient hardness after the printing process.

3.3.2. Carrier Solvent

The carrier solvent constitutes the bulk of the ink solution, which mainly determines the ink properties such as viscosity, surface tension, stability, density, and evaporation rate. It also dissolves and disperses the metal species and other additive components. The carrier solvents can be categorized into aqueous (or water-based) and non-aqueous solvents.

Aqueous inks consist of functional species, catalyst nanoparticles (or metal precursors in our case), and some additives dissolved/dispersed in water. Aqueous inks usually have lower viscosity and evaporation rate, and higher surface tension compared to their non-aqueous counterparts. However, these properties can be tuned to meet the specific inkjet printer requirements by using co-solvents such as alcohols, glycols, and surfactants (Maleki & Bertola, 2020). Water is often used in the printing industry as the carrier solvent in aqueous inks due to its safety and availability; however, water-based inks have slow drying rates on non-porous substrates such as glass and steel (Feys et al., 2012). In addition, they exhibit relatively low stability for dispersed metal nanoparticles (Gebauer, Mackert, Ognjanović, & Winterer, 2018).

Solvent-based inks use organic solvents such as short chain alcohols (e.g., ethanol, isopropanol, glycols) and toluene as carrier fluid. This class of inks is usually selected to improve the ink stability, lower the surface tension, or increase the viscosity and the evaporation rate (X. Liu et al., 2015). One factor in the choice of solvents is the optimum drying rate. Using slow-drying solvents would increase the drying time and energy required. On the other hand, volatile solvents would reduce the solvent removal time and ease the multilayer deposition process; however, fast solvent evaporation at the nozzle may cause clogging. One approach is to use a mixture of solvents to optimize the evaporation rate (Maleki & Bertola, 2020). The solvent interaction with the substrate should also be considered as it affects adhesion and print quality. By choosing a suitable solvent, the formulated inks can be deposited onto various substrates with enhanced print quality and uniformity.

3.3.3. Functional Species Precursor

Catalyst species used as functional precursors can appear in the form of either colloidal catalyst nanoparticles or metal-based solutions in the ink medium. The colloidal nanoparticles in the solution could be the result of direct synthesis (e.g., sol–gel method), or could be added and dispersed as dry nanopowders.

3.3.3.1. Catalyst-Based Solutions

In this approach, catalyst based compounds such as metal salts are dissolved in the carrier solvent to produce stable ink solutions (X. Liu et al., 2015). This process is relatively simple, and the formulated inks can be used continuously in the inkjet printing system without the risk of nozzle blockage. Furthermore, inkjet printing is a part of the synthesis process, and printed layers will be converted to metal oxides by heat-treatments or post-reactions. In other words, catalyst materials would be synthesized and immobilized through a simple one-stage process. Furthermore, the growth of metal oxides on the substrate may produce various material structures.

Parkinson et al. (Rodríguez-Gutiérrez et al., 2018; Seley, Ayers, & Parkinson, 2013; Skorupska et al., 2015) developed libraries of electrocatalysts (e.g., Cr, Fe, Cu, Pt, Ru, Ir) for oxygen evolution reaction via combinatorial studies using the inkjet printing technology. Metal salt precursors (e.g., metal nitrates and chlorides) were added to the ink solutions containing water and glycols. The formulated inks were then printed onto the substrate using a lab-scale inkjet printer. The printed layers were converted to mixed metal oxides under air pyrolysis process. After kinetic studies, the optimised electrocatalysts were obtained and further characterized.

Hu et al. (Maleki & Bertola, 2020) used the inkjet printing method for the direct synthesis and fabrication of platinum catalysts by using a chloroplatinic solution as catalyst precursor. The chloroplatinic acid solution was added to water/ethylene glycol as a carrier solvent and then sent to a commercial microdispensing system. After printing, the coated substrates were placed in a furnace under methanol flow at 250 °C to produce the platinum catalyst.

3.3.4. Additives

Additives are ingredients such as surfactants, co-polymers, dispersing agents and acids/bases added to the ink solutions in small amounts for different purposes. Surfactants such as Abesone and Triton X-100 act as dispersing agents and reduce the surface tension of metal oxide colloidal solutions (Kralova, Dzik, Vesely, & Cihlar, 2014; Nguyen, Chen, & He, 2014). Co-polymer macromolecules such as polyethylene glycol (PEG) are used to increase the layer uniformity and prevent cracking during the post thermal treatments (J. Yu, Zhao, Zhao, & Wang, 2001). They also hinder the coffee ring effect caused by the capillary flow of particles from the droplet centre to the evaporation interface (Seo, Jang, Chae, & Shin, 2017). The use of an acidic medium (e.g., HCl, HNO_3) maintains the pH and generates a repulsive charge on the particle surface leading to stabilization of dispersed metal oxide nanoparticles (Gebauer et al., 2018; Maleki & Bertola, 2019). Despite the efforts to utilize inkjet printing technology for inorganic materials, synthesis and development of stable jettable inks still remain the principal challenge. Therefore, further studies are required to make progress in this area.

3.4. Nickel-Based Multi-Metal Oxides

Nickel based systems are the most studied catalysts for the OER in alkaline media. Ni oxides/hydroxides (Oliver-Tolentino et al., 2014; X. Yu, Zhang, Yuan, & Shi, 2015), Ni chalcogenides (Anantharaj, Kennedy, & Kundu, 2017), Ni phosphides (Pan et al., 2015; L. Yan et al., 2017), and Ni nitrides (Y. Wang, Zhang, Pan, Ma, & Zhang, 2017; F. Yan et al., 2017; Zhuoxun Yin et al., 2017) are reported to exhibit good electrochemical performance toward the OER. Doping other transition metals (Fe, Co, Al, Ce, etc.) into the nickel lattice is the most adopted strategy to further enhance the activity. Among these, nickel−iron (oxy)- hydroxides excel as prime electrocatalyst candidates through their low overpotentials, abundance, and low cost (Gong & Dai, 2015; Görlin et al., 2017; X. Lu & Zhao, 2015; W. Ma et al., 2015; Song & Hu, 2014; Swierk, Klaus, Trotochaud, Bell, & Tilley, 2015; Trotochaud, Young, Ranney, & Boettcher, 2014). Corrigan first recognized the influence of adventitious iron incorporation and proposed that Fe increases the conductivity of NiOOH (Corrigan,

1987). Boettcher and co-workers found that intentional or incidental incorporation of Fe significantly enhances the catalytic activity of nickel (oxy)hydroxide (Trotochaud et al., 2014). They showed that iron affects the electronic structure of NiOOH and exerts partial charge transfer activation on Ni. Louie and Bell validated that Fe in NiOOH modifies the Ni-O local environment, improving activity (Louie & Bell, 2013). The synergism between Ni and Fe centers is well established by various studies (Fominykh et al., 2015; Görlin et al., 2016; Landon et al., 2012; Oliver-Tolentino et al., 2014; Yeo & Bell, 2012). However, the optimum doping of Fe has been inconsistently reported between as low as 10% (Landon et al., 2012; Xiaohong Li, Walsh, & Pletcher, 2011) and as high as 50% (Corrigan, 1987), which calls for a systematic investigation.

Higher order composition spaces hold great promise of improved electrocatalytic performance. Incorporation of Fe is shown to have an electron withdrawing effect on Ni, inducing an anodic shift of the redox couple to one with more oxidizing power and, therefore, faster OER kinetics (Trotochaud et al., 2014). In an effort to study this partial charge transfer activation by the doping of other transition metals, ternary oxides of nickel, iron, and cobalt have been deliberately studied (Bates, Jia, Doan, Liang, & Mukerjee, 2016; Gerken, Shaner, Massé, Porubsky, & Stahl, 2014; Inamdar, Chavan, Pawar, Kim, & Im, 2020; Stevens et al., 2019; Vandichel, Busch, & Laasonen, 2020; A.-L. Wang, Xu, & Li, 2016; T. Wang, Xu, & Wang, 2017; Xiao, Lu, & Zhao, 2014; Zhao et al., 2016). Addition of Co is expected to render improved electrical conductivity and affect electronic structure, tailoring the activation energies of key steps in the catalytic cycle. Also, it has been reported that an iron content beyond 25% in Ni-Fe catalysts induces the formation of segregated FeOOH islands, whereas it takes 50% of iron in Co-Fe catalysts for such a phase segregation to occur (Friebel et al., 2015). The presence of cobalt could, therefore, allow increased iron incorporation, generating more active sites (T. Wang et al., 2017). The positive effect of partial charge transfer activation becomes compromised at a composition prone to phase segregation and loss of electrical interconnection. In this regard, we will try to arrive at an optimal composition with a fine balance between the two.

3.5. Experimental

3.5.1. Materials

Inkjet buffer ink for metal salts were supplied from Sağlık İzleme Sistemleri A.Ş. (SIZ+). Corresponding metal salts were added to conduct experiments. $Ni(NO_3)_2.6H_2O$, $Mn(NO_3)_2.4H_2O$, $Co(NO_3)_2.6H_2O$, $Cu(NO_3)_2.2.5H_2O$, $Fe(Cl_3)_3.6H_2O$, $Cr(NO_3)_3.9H_2O$ and Ethanol (96%) were purchased from Chempure Private Limited, Sigma-Aldrich, Tekkim and Merck. SIZ+ Inkjet Material Printer was supplied from SIZ+ for deposition procedures.

3.5.2. Methods

3.5.2.1. Ink Formulation

In literature ink formulation was given as follows 10 mmol metal nitrate salt was dissolved in 60 mL ethanol then 40 mmol acetic acid and 12 mmol HCl were added to increase solubility and finally 1.6 g F-127 were added to mixture (Xiang et al., 2014). Inks solutions were stirred for 30 min. However, inks which prepared with this formula have not satisfy the required viscosity for commercial Epson® printer head. So, we developed our own ink formulation with a slight change.

In our formulation we added glycerol to increase viscosity of inks. 10 mmol metal nitrate salt was dissolved at 52 mL ethanol and 8 mL glycerol solution. Glycerol was added to arrange the viscosity of inks. Then 15-20 mL acetic acid was added to increase solubility. Finally 1.6 g F-127 was added to mixture.

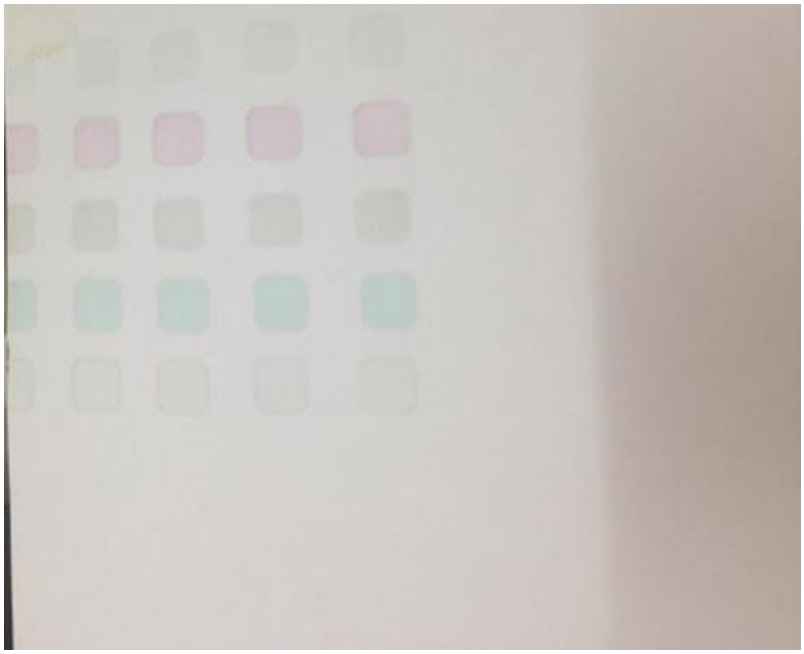

Figure 3. 2. Square prints with inks we have prepared using our own ink formulation. Fe, Co, Cr, Cu and Ni inks from top to bottom, respectively.

3.5.2.2. Characterization of Inks

3.5.2.2.1 Viscosity Measurements

Viscosity measurements were taken with NDJ-1 viscosimeter. In order to measure viscosity values correctly, #0 rotor was used. Firstly, viscosity values of ethanol+glycerol mixture was measured to compare our results with literature. Units are mPa/sec. For all measurements.

Figure 3. 3. The experimental setup for viscosity measurement of precursor inks.

Table 3. 2. Viscosity measurements of catalyst precursor inks.

Name of Solution	**Viscosity (mPa/sec)**
Ethanol + glycerol	5
Chromium ink	6
Copper ink	4
Cobalt ink	4
Iron ink	4.75
Nickel ink	4.25
Manganese ink	4

3.5.2.2.2 Surface Tension Measurements

Measurements were taken with Krüss K10 ST tensiometer device. Surface tension results are determined by De Noüy ring method. Results are indicated as dyn/cm. Before taking measurements, digital display should be zero. Then, ring that is made of platinium is dipped into the sample. After this step, device is run by pressing run button. Results are shown when the ring is separated from sample as dynes/cm.

Figure 3. 4. The experimental setup for surface tension measurement of precursor inks.

Table 3. 3. Surface tension measurements of catalyst precursor inks.

Metal Nitrate Salt	In literature	Our solution
Cu	21-22	24.1
Cr	21-22	23.9
Ni	21-22	23.7

Cont. on the next page

Cont. of Table 3.3

Mn	21-22	24.6
Co	21-22	23.7
Fe	21-22	24.8
Metal Nitrate Salt	In literature (only ethanol and glycerol mixture does not include metal salt)	Our solution (EtOH + Glycerol+AcOH+ salt)
Cu	23.5	25.9
Cr	23.5	27.2
Ni	23.5	26.4
Mn	23.5	24.8
Co	23.5	26
Fe	23.5	25.8

3.5.2.3. Calcination of Metal Oxide Catalysts

NiO, Mn_3O_4, Cr_2O_3, Co_3O_4, CuO and Fe_2O_3 catalysts were printed with Epson® Inkjet Material Printer. To test precision, samples were printed for each catalyst, calcined at 40˚C for 18 h, at 70˚C for 24 h, at 350˚C for 10 h, respectively.

3.6. Results and Discussion

3.6.1. SEM Measurements

The surface morphology of the deposited films was studied by SEM. Images were taken from various points on the trimetallic NiFeCo sample (Figure 3.6.). An

image from one point of the sample ($Ni_{90}Fe_5Co_5O_x$) is shown in Figure 3.7. A dense, compact structure with a continuous distribution of particles can be observed.

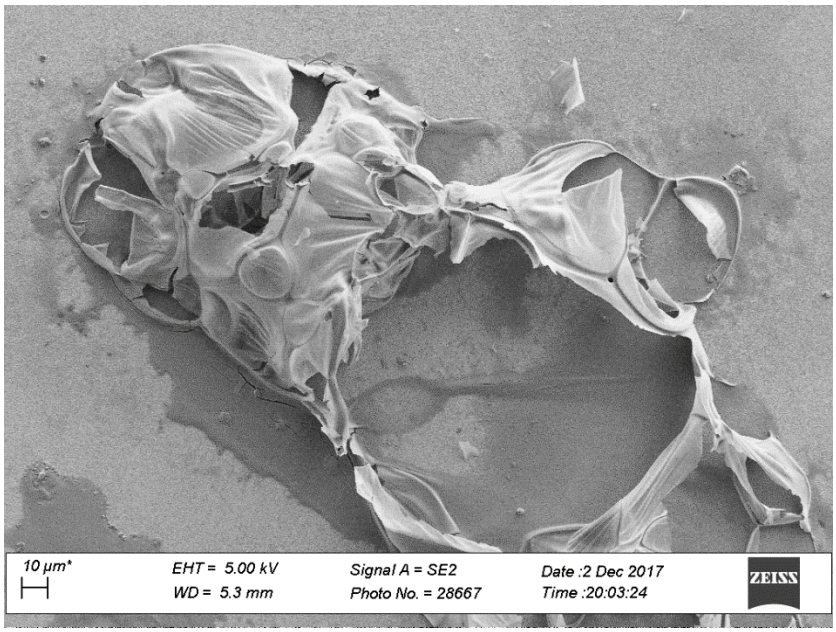

Figure 3. 5. SEM images of trimetallic NiFeCo sample.

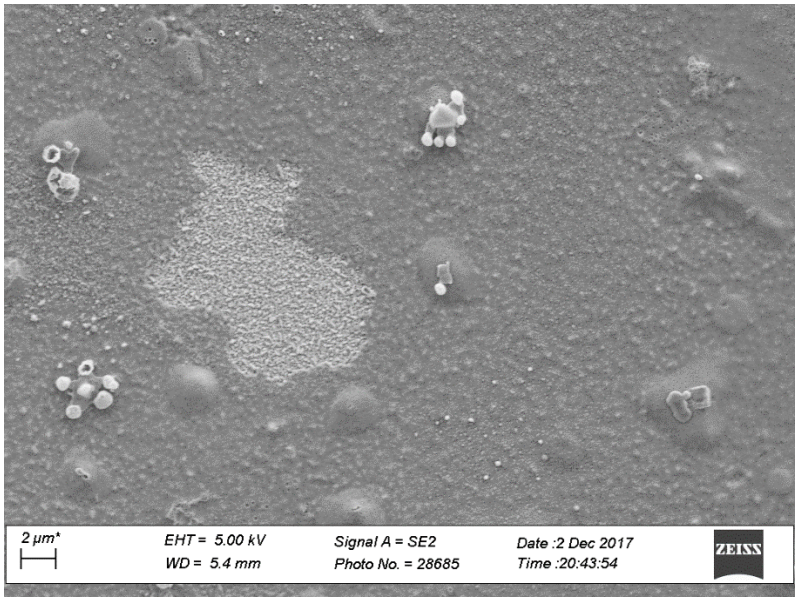

Figure 3. 6. SEM images of trimetallic $Ni_{87}Fe_7Co_6O_x$ sample.

CHAPTER 4

OXYGEN ACTIVATION ON BA-CONTAINING PEROVSKITE MATERIALS

4.1. Introduction

Oxygen exchange reactions, including oxygen reduction reaction (ORR) and oxygen evolution reaction (OER), occurring at gas-solid interfaces are vital to the process of energy conversion in metal-air batteries (Lyu et al., 2017), solid oxide cells (SOCs) (Duan et al., 2018; Hauch et al., 2020; Othman, Droushiotis, Wu, Kelsall, & Li, 2011; Yang et al., 2009), water splitting (Y. Zhu, Zhou, Zhong, et al., 2017), and catalytic membrane reactors (Jia, He, Zhang, Caro, & Jiang, 2021). The activation mechanism of oxygen at gas-solid interfaces is still unclear, because the complex four-electron transfer process is related to various oxygen species, evolving with the material composition and structure, as well as the reaction conditions (W. T. Hong et al., 2015; R. Ma et al., 2019; Suen et al., 2017; Suntivich, May Kevin, Gasteiger Hubert, Goodenough John, & Shao-Horn, 2011; Y. Zhu, Zhou, & Shao, 2017). Elucidating the oxygen activation mechanism is of great significance for the design and preparation of new materials with high activity for energy conversion devices. Although notable advances have been achieved in recent decades, a multitude of ambiguous relationships between researches of experiments and theory still need to be disclosed.

Transition metals, such as Mn, Fe, Co, and Ni, in the B-sites of perovskite-type oxides ($ABO_{3-\delta}$) are generally considered as active sites because both the mixed valence states of the transition metals and medium B─O bond length are favorable for oxygen activation (D. Chen, Chen, Baiyee, Shao, & Ciucci, 2015; Huang, Pellegrinelli, & Wachsman, 2017; Rupp, Opitz, Nenning, Limbeck, & Fleig, 2017; Rupp et al., 2015; Sun et al., 2019; Suntivich, Gasteiger, et al., 2011; Y. Zhu, Zhou, & Shao, 2017). However, the segregation of alkaline earth elements, i.e., Ba, Sr, and Ca, in the A-sites of perovskites and double perovskites in an oxygen-enriched atmosphere has been widely reported (Druce et al., 2014; S. P. Jiang, 2007; Jung & Tuller, 2012; Y. Li et al.,

2017; Y. Liu et al., 2013; Tian et al., 2021; Wei, Schroeder, & Martin, 2018; L. Zhu et al., 2016). The degradation of electrode catalytic activity was even suggested to closely correlate to the segregation of alkaline earth elements on perovskite surfaces (Druce et al., 2014; Jung & Tuller, 2012; Y. Liu et al., 2013; Tian et al., 2021; L. Zhu et al., 2016). The segregation tendency of alkaline earth elements is directly related to cationic size (Kwon, Lee, & Han, 2016; Lee, Han, Chen, Cai, & Yildiz, 2013). Ba is easier to segregate on the perovskite surface compared to other alkaline-earth and lanthanide elements. An interesting phenomenon that perovskite-type materials containing Ba in A-sites have outstanding activity toward oxygen activation compared to materials with similar structures and compositions. Several studies indicated that the catalytic activity of perovskites can be markedly improved by introducing $BaCO_3$, although $BaCO_3$ was regarded as an inert matter toward oxygen exchange reactions (Gao, Meng, Lee, Tong, & Brinkman, 2019; Hong, Chen, & Xia, 2015). Therefore, the authentic character of A-site elements toward the oxygen activation process remains a debate, especially the role of Ba in the oxygen exchange reactions of Ba-containing materials.

$Ba_{0.5}Sr_{0.5}Co_{0.8}Fe_{0.2}O_{3-\delta}$ (BSCF), which is widely investigated in energy conversion processes, is chosen because of its high catalytic activity toward oxygen activation. Kinetic analysis shows that the oxygen exchange rates can be significantly improved by increasing the Ba content in $Ba_xSr_{1-x}Co_{0.8}Fe_{0.2}O_{3-\delta}$ (x = 0, 0.1, 0.3, 0.5, and 0.7).

4.2. Perovskite Oxide Catalysts

The latest researches are focused on multi-metal oxides for their high abundance and good catalytic activities. One class of multi-metal oxide is highly investigated due to their flexibility of chemical and physical properties. The general formula of perovskites is ABO_3. An ideal ABO_3 type perovskite has cubic symmetry with a pm3m space group. A site is occupied by an alkaline earth element in 12-fold coordination and the B site is occupied by a transition metal element in 6-fold coordination to the oxygen atoms. Deviations from cubic symmetry can be observed in orthorhombic, rhombohedral, or tetrahedral symmetry formations. Generally, the B site of the perovskite is identified as an oxygen evaluation reaction center. There is no detailed information about the mechanism of hydrogen evaluation and oxygen evolution

reactions of perovskites. According to the latest studies, HER and OER efficiency stabilities, Fermi level, bandgap energy, and the density of states in conduction and valence bands of perovskites can be improved by dopants either to A site or B site.

BSCF is a $SrCoO_{3-\delta}$ type perovskite which was firstly developed for high temperature oxygen permeation membrane applications. Based on Shao's studies, introducing Ba and Sr atoms in 50% percentage to $Co_{0.8}Fe_{0.2}$ provided the best stability for perovskite structure and gained it remarkable oxygen permeation properties. By doping $Co_{0.8}Fe_{0.2}$ structure with Ba and Sr atoms, oxygen vacancies increased therefore increasing its performance (Shao, Xiong, Tong, Dong, & Yang, 2001).

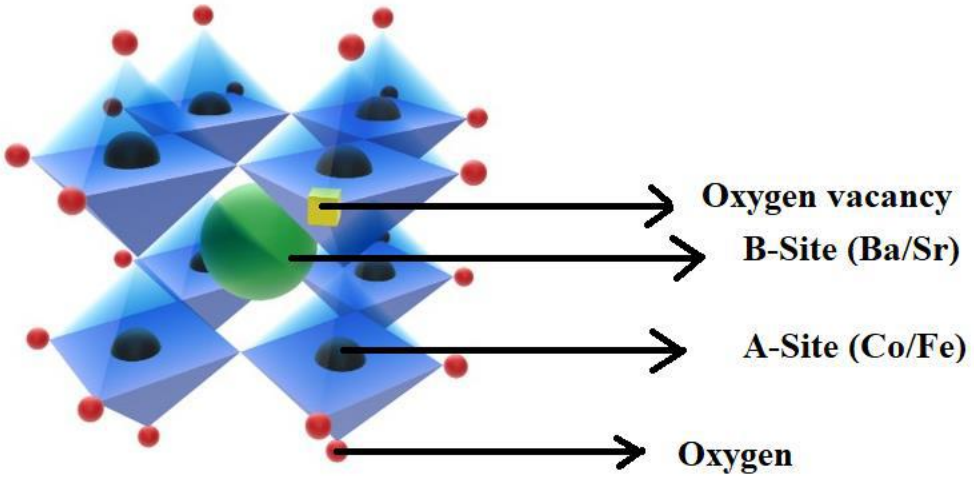

Figure 4. 1. ABO_3 type perovskite structure showing A-Site and B sites atoms with oxygen vacancy.

BSCF was firstly first use as an energy material is for fuel cell applications by Shao and Haile. In this study, BSCF has shown to be a promising candidate as cathode material for its ORR activities (Shao & Haile, 2004). Fe doping effects was investigated by Chen et al. and they found that $Ba_{0.5}Sr_{0.5}Co_{1-y}Fe_yO_{3-\delta}$ cathodes at y = 0.2 showed the best ORR catalytic activity and increase in Fe percentage concludes in decrease of electrical conductivity (Z. Chen, Ran, Zhou, Shao, & Liu, 2007). Molecular dynamic simulation studies done by Fisher et al. proved that the 50 % percentage doping of Ba Sr atoms conclude in the best oxygen vacancy content and ionic conductivity (Fisher et al., 2007).

In the later researches, for its high electrochemical performance BSCF is considered for water splitting catalysts too. According to studies of Suntivich et al.

BSCF shows better current densities than state-of-art IrO_2 for oxygen evolution reactions (Suntivich, May Kevin, et al., 2011).

Activity of BSCF towards ORR and OER reactions can be tuned by electrode preparation techniques. Fabbri et al. showed that addition of acetylene black to electrode coating material can boost BSCF activity by chancing the electronic configuration. Change in electronic configuration of BSCF is caused by the reduction of Co oxidation (P. F. Liu et al., 2020) states by carbon addition (Fabbri, Nachtegaal, Cheng, & Schmidt, 2015). In further studies, Fabbri et al. also showed the effect of ball milling of perovskite powder enhances its OER activity by providing smaller crystalline sizes (Cheng, Fabbri, Kim, Nachtegaal, & Schmidt, 2017). Another work on electrode preparation was done by using Ni foam and ITO as substrate and chancing the film thickness of BSCF on Ni foam. Increase of film thickness enhanced the durability of catalyst in alkaline media and the study proved that Ni foam serves as a better substrate by tuning the oxidation states of perovskite for OER (G. Chen et al.).

Hydrogen evolution catalyst characteristics of perovskites was not investigated in detail in alkaline solutions due to complicate HER mechanisms and overpotential losses due to slow kinetics of reaction. Xu et al. firstly investigated the HER activity of BSCF and Pr doped BSCF for its known OER popularity among perovskites and showed that Pr doped BSCF has 237 mV overpotential at 10 mA cm^{-2} and BSCF showed 342 mV overpotential. This drop in overpotential is explained in facilitated electron transfer by Pr doping and proved that BSCF is a promising candidate as a HER catalyst (Xu, Chen, et al., 2016). Li, Xiangnan et al reported the HER activity dependency of BSCF to Ba^{+2} ions. According to their study, Ba^{+2} ion deficiency doping improved electrochemical and physical properties in addition of Zr and Y atoms to structure by showing smaller Tafel slopes and lower overpotentials in alkaline media (Xiangnan Li et al., 2018).

Several synthesis routes was studies for perovskites such as sol-gel synthesis (Behrouzifar, Asadi, Mohammadi, & Pak, 2012; Kautkar, Shirbhate, & Acharya, 2018), solid state reactions (Hung & Laing, 2009), co-precipitation and hydrothermal synthesis, flame spray synthesis (Fabbri et al., 2017; Heel, Holtappels, Hug, & Graule, 2010), solution combustion synthesis (Deganello, Liotta, Marcì, Fabbri, & Traversa, 2013), glycine nitrate process concluding different crystalline sizes, surface and bulk characteristics and therefore ionic conductivity, OER/ORR/HER activities. Among these methods, Sol-Gel synthesis by EDTA-citrate complexing method is the most

commonly used route for providing homogeneity on molecular level which enhance electrochemical performance and fast reaction kinetics.

Laing et al. compared solid state reaction, Pechini method and sol-gel synthesis of BSCF in their studies and reported that the BSCF synthesized by sol-gel method has higher conductivities by 90% than solid state reaction and 42% Pechini method (Hung & Laing, 2009).

Xu et al. synthesized BSCF as a membrane material to test the differences on oxygen permeability performance caused by synthesis methods. In the study, they compared solid-state reaction, modified citrate process and EDTA - citrate complexing method. They observed that the smallest grain size was obtained by EDTA-citrate method with 0,1 μm.

May et al. studied the structural effects on electrochemical activity of BSCF in alkaline media and they showed that surface amorphization increased with increasing cycling number leading to better catalytic activities for OER (May et al., 2012).

The significant variations in the electrochemical activity of BSCF emerge from different synthesis and calcination methods, which directly affect the morphology and surface area of the structure. Furthermore, differences in electrode preparation give rise to inconsistencies about the OER activity of BSCF (Xu, Pan, et al., 2016).

Silver, with its highest electrical conductivity, is the most abundant and cheapest noble metal (Z. Li et al., 2019; Xia, 2019; Y. Zhou et al., 2015). In addition, silver nanoparticles show excellent stability in basic solutions (R. Liu et al., 2015). An increase in electrochemical performance of catalysts that modified with silver, is expected (Zhuang et al., 2011). Silver has high activity for oxygen reduction and evolution reactions (Ananth, Manimaran, Arul Raj, & Sureka, 2007; Wagner, Schulze, & Gülzow, 2004), and this is likely to provide additional benefits to catalysts. Hence, the addition of silver is an ideal option to improve the electrochemical activity of BSCF.

In this study, we demonstrate the electrochemical catalytic performance and stability of silver doped-BSCF (BSCF-Ag) perovskite structure to observe whether there is an increase in these properties. There are lots of studies on solid oxide fuel cells related to silver doped-BSCF (Chatrchyan et al., 2014; Leo, Liu, & Diniz da Costa, 2009; Liang, Zhou, Li, & Zhu, 2013; Lin, Ran, & Shao, 2010; Mosiałek et al., 2018; Park, Lee, Dorris, Park, & Balachandran, 2012; Yusop, Huai, Rahman, Baharuddin, & Raharjo, 2020; Zhang, Liu, Huang, Lu, & Su, 2008; W. X. Zhu, Lü, Wang, Guan, &

Zhang, 2011). However, as far as we know, the effects of silver doping on BSCF for investigating OER activity have not been studied. Additionally, we compared the electrochemical activities of BSCF and BSCF-Ag. BSCF and BSCF-Ag were synthesized by using the sol–gel process. All perovskite structures were calcined under the same conditions. BSCF-Ag exhibited higher electrochemical performance than BSCF. Characterization of these perovskite structures was presented by using XRD, SEM, EDX, and XPS.

4.3. Experimental

4.3.1. Synthesis of BSCF Perovskite Structure

Ethylenediaminetetraacetic acid (EDTA)-citrate method was used to synthesize the BSCF perovskite structures. The nitrate salts of Ba, Sr, Co, Fe, and Ag for the respective doped BSCF powder were dissolved in deionized water, stoichiometrically. $AgNO_3$ was added to achieve a silver ratio of 1% by weight in total. Complexing agents EDTA and citric acid were then added to the prepared solution, and the molar ratio was 1:1:2. To adjust pH to ~ 5, NH_4OH was added for complexation. The final solution was stirred for 24 h at 70 °C with 400 rpm until the gelation entirely occured. The obtained gelled samples were dried at 250 °C for an extra 24 h. Lastly, the collected material was calcinated at 1000 °C for 12 h to obtain the perovskite powder. Catalyst inks were prepared by using as-synthesized powders to use in the fabrication of the electrodes. A dispersion of 10 mg of synthesized perovskite powders and 10 mg carbon black were mixed with 100 µl of Nafion® and 1 ml of ethyl alcohol, and then the mixture was sonicated for 30 min to obtain catalyst inks.

4.3.1.2. Electrochemical Measurements

Perovskite powders were coated on FTO glasses by using a drop-casting method. Firstly, FTO-coated glasses of 1 × 1 cm^2 were prepared. Then, the dispersed catalyst ink was coated onto the FTO surface with the loading of ~ 232 µg/cm^2. Coated glasses were annealed at 80 °C for 2 h. Cyclic voltammetry and linear sweep

voltammetry measurements (LSV) were carried out by using the Metrohm PG-208 instrument. As reference and counter electrodes Ag/AgCl and Pt mesh were used, respectively. All the electrochemical measurements were performed in 1.0 M KOH solution. LSV measurements were done between 1 and 1,9 V vs. RHE.

Chronopotentiomemtric measurements were carried out at a constant current density of 10 mA cm^{-2} to determine the stability of catalysts.

4.3.3. Results and Discussion

4.3.3.1 Materials Structure & Morphology

To decide the phases of BSCF and BSCF-Ag, we used X-ray diffraction (XRD) and Rietveld refinement analysis. In calcination temperatures below 700 °C, no characteristic diffraction peaks of Ag were found due to uniform dispersion over the surface of BSCF grains (W. Zhou et al., 2008). Figure 4.2. shows that a single crystallized perovskite structure was produced with the sol–gel method after a calcination process under air at 1000 °C for 12 h. Scherrer equation was used to determine the crystal size of BSCF-Ag and it was calculated as 32 nm. With the markers used, Fig. 1 shows the peaks arising from the introduction of silver into the perovskite structure. All diffraction peaks can be classified finely based on the cubic perovskite phase of BSCF. Ag and AgO phases were not observed. This indicates that silver is distributed uniformly in the spaces on the BSCF surface. No other peaks caused by impurities were detected. Rietveld refinement analysis results suggest that both BSCF and BSCF-Ag perovskite structures have cubic structure and similar lattice parameters. As shown in Table 4.1., Rietveld refinement results have a low-reliability factor, which indicates that the fitting of these results was reasonably good.

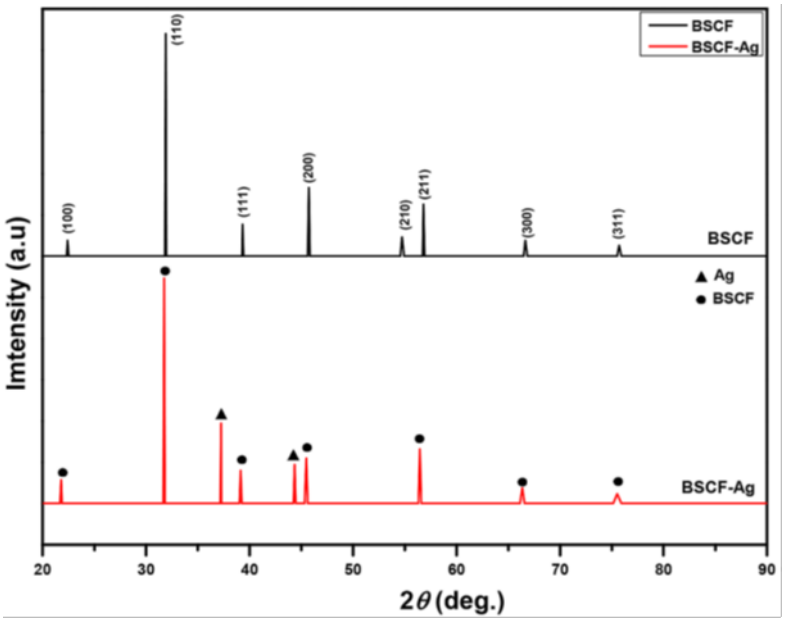

Figure 4. 2. XRD patterns of BSCF and BSCF-Ag powders

Table 4. 1. Rietveld refined parameters and reliability factors of perovskites

Perovskites	Space group	Lattice parameter	X^2	R_p (%)	R_{wp} (%)
BSCF	*P*m-3 m	a = 3.992	1.978	3.10	5.44
BSCF-Ag	*P*m-3 m	a = 3.989	1.434	3.18	4.94

SEM images of perovskite structures are shown in Fig. 4.3. The porous size of BSCF is larger than BSCF-Ag, however, after modified Ag ion, this porous size has started to shrink. This show us that BSCF is successfully modified with Ag ion and Ag ion enters in holes which is found at BSCF in Fig. 4.3.a. Besides, the surface is rougher at BSCF-Ag due to the aggregation of silver particles and decomposition of the perovskite surface, also it is seen that Modified-Ag particles are very clear in Fig. 4.3.a. In the Table 4.2., EDX results of BSCF-Ag structure was shown. According to the EDX results, the amount of silver was in the desired ratio. To determine the specific surface area of BSCF and BSCF-Ag with BET, we used the nitrogen (N_2) sorption measurement method. Characteristic profiles of mesoporous structures were shown in both isotherms of perovskite materials. The specific surface area (S_{BET}) of BSCF and BSCF-Ag were measured 0.77 m^2g^{-1} and 1.85 m^2g^{-1}, respectively.

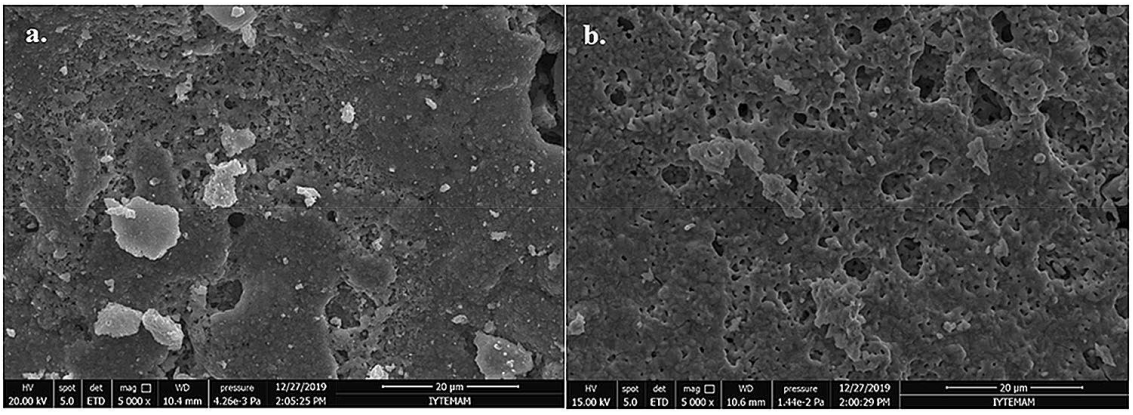

Figure 4. 3. SEM images of a BSCF-Ag and b BSCF perovskite oxides

Table 4. 2. Chemical composition of BSCF-Ag perovskite structure resulting from the EDX analyzes

Element	**Wt%**
O	25.09
Fe	2.57
Co	14.06
Sr	18.07
Ag	0.96
Ba	39.25

To decide the contents of perovskite structures X-ray photoelectron spectra (XPS) was used. XPS of BSCF and BSCF-Ag perovskite structures were shown in Fig. 4.4. Characteristic peaks for barium, cobalt, and oxygen are present intensely. At binding energies 775 and 792 eV, peaks of Ba $3p_{1/2}$ can be observed. Differentiating these peaks from Co peaks are difficult due to overlapping. The less intense peaks of Sr

and Fe can be observed at 256 eV and 711 eV, respectively. Moreover, the peak of silver can be determined at 365 eV for the spectra of BSCF-Ag.

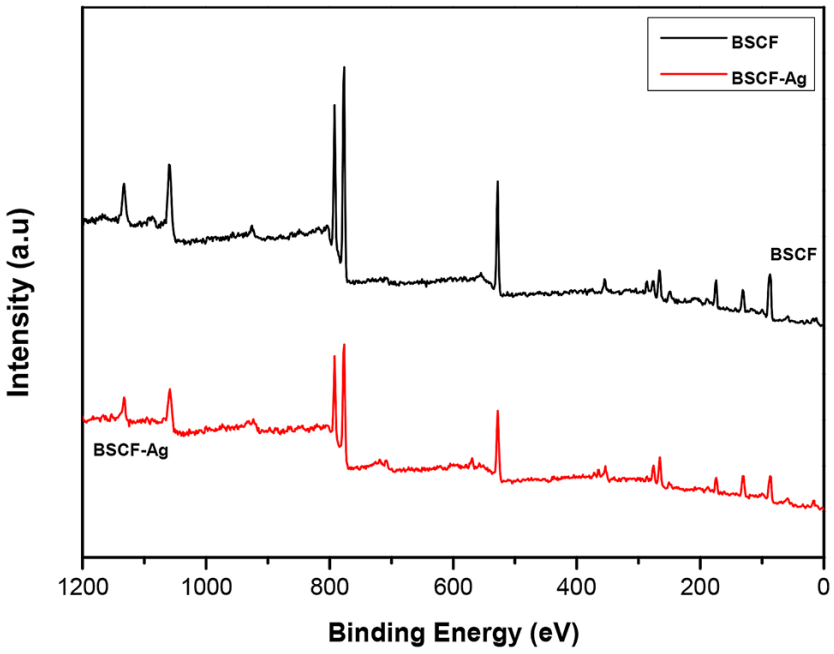

Figure 4. 4. X-ray photoelectron spectroscopy (XPS) spectra of BSCF and BSCF-Ag

4.3.3.2 Oxygen Evolution Reaction Performance

To measure linear sweep voltammograms (LSV) (Fig. 4.5.a) of BSCF, and BSCF-Ag, we used a 3-electrode system in 1.0 mol L^{-1} KOH solution with a scan rate of 10 mV s^{-1} over the OER portion. The onset potential of state-of-art catalyst IrO_2 is 1.4 V vs. RHE (Felix, Bladergroen, Linkov, Pollet, & Pasupathi, 2019). BSCF-Ag exhibited an onset potential of 1.51 V vs. RHE, which is a good OER onset potential. Additionally, BSCF-Ag showed a better OER performance than pure BSCF.

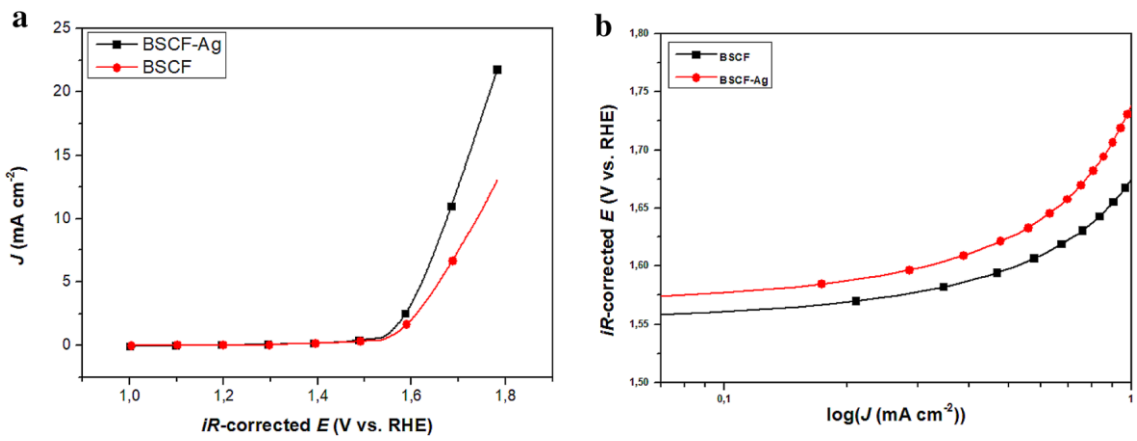

Figure 4. 5. LSVs for a BSCF and BSCF-Ag and b Tafel plots for perovskite structures between 0.1 and 0.5 mA cm^{-2}

An essential term for electrochemical solar fuel synthesis is overpotential (η), which specifies the necessary excessive potential to achieve the current density of 10 mA cm^{2-} (McCrory, Jung, Peters, & Jaramillo, 2013). Comparing the overpotentials of the as-synthesized catalysts at the specific current density of 10 mA cm^{2-}, the difference of theoretical reversible potential (1.23 V vs. RHE) and the significant potential to reach 10 mA cm^{2-} for OER is used to define overpotential in this study. The overpotential for BSCF-Ag to achieve 10 mA cm^{2-} current density is 0.44 V. This overpotential is lower than the overpotential of BSCF but higher than the overpotential of IrO_2, which are 0.51 V and 0.32 V (McCrory et al., 2013) respectively. In Table 4.3 we showed mass activity (MA) and specific activity (SA). The MA value of BSCF-Ag is 93.78 Ag^{-1}_{cat} at a 550 mV overpotential (η). This value is higher than for BSCF (56.39 Ag^{-1}_{cat}). This value shows that BSCF- Ag has higher OER activity than pure BSCF. In Fig. 4.5.b Tafel plots of BSCF and BSCF-Ag are demonstrated. The Tafel slope value for BSCF-Ag was less high than pure BSCF, which confirms that BSCF-Ag has faster kinetics than pure BSCF.

For practical applications, long term performance stability is an important factor. The performance stability of BSCF-Ag and BSCF were measured by using the chronopotentiometric (CP) test in a 1 M KOH solution. The CP tests were carried out in a 3-electrode cell. Catalyst ink was deposited on a FTO-coated glass with a dimension of 1 cm × 1 cm to reach a catalyst loading of 0.232 mg cm^{-2}. Figure 4.6. represents the long-term stabilities of BSCF powders for OER. Chronopotentiometric measurements were carried out at a constant current density of 10 mA cm^{-2} in 1.0 M KOH solution. Although both perovskite structures were very stable for 10 h, the BSCF-Ag structure

has achieved this current density at a very low potential value, which also indicates its lower overpotential as an OER catalyst.

Table 4. 3. Summarization of OER performances of BSCF and BSCF-AG perovskite structures.

Sample name	BET surface area ($m^2 \cdot g^{-1}$)	Overpotential at 10 $mA \cdot cm^{-2}$	Onset potential (V)	MA at 0.55 V ($A \cdot g^{-1}$)	SA at 0.55 V ($mA \cdot cm^{-2}$)	Tafel slope ($mV \cdot dec^{-1}$)
BSCF	0.77	0.51	1.54	56.29	7.3	281
BSCF-Ag	1.85	0.44	1.51	93.78	5.07	122

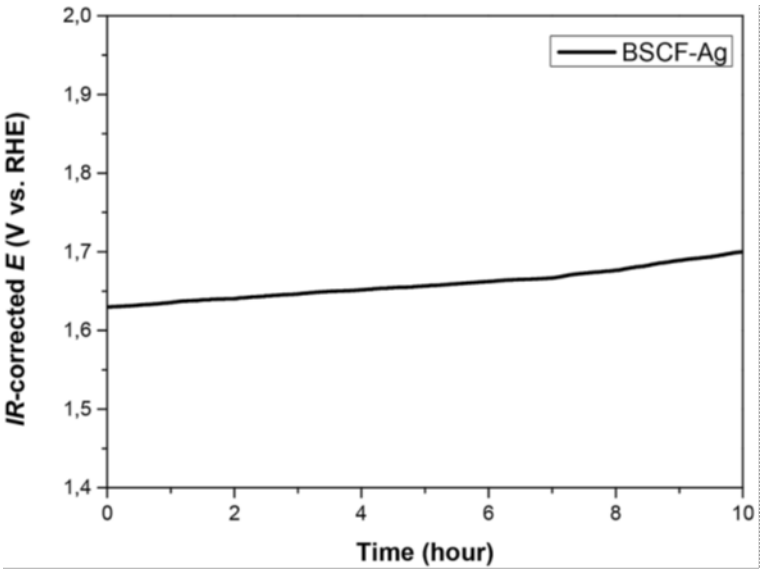

Figure 4. 6. Chronopotentiometric measurements of BSCF-Ag and BSCF maintaining a constant current density of 10 mA cm^{-2} in a 1 mol L^{-1} KOH solution

Lastly, we investigated the oxidation state of BSCF perovskite structures. For oxygen evolution reaction (OER), it is known that the greater amount of Co^{2+} leads to a shift towards higher binding energies (Wen, Zhang, He, Yu, & Teraoka, 2007; Xu, Pan, et al., 2016). Besides, it was shown that if Co^{2+} content of the perovskite structure has larger, its electrochemical activity as an OER catalyst is enhanced (Fabbri et al., 2017). Because of overlapping between Co 2p and Ba 3d lines deciding the surface oxidation evolves into a tough challenge (Norman & Leach, 2011; Xu, Chen, et al., 2016). In Fig.4.7., it can be seen that there is a shift towards higher binding energies for BSCF-Ag, which is the result of larger Co^{2+} content.

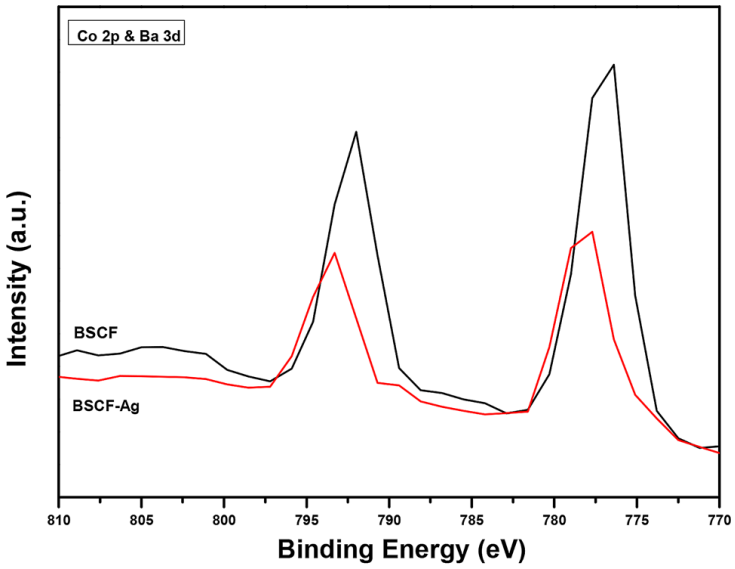

Figure 4. 7. XPS spectra of Co 2p and Ba 3d for BSCF-Ag and pure BSCF

CHAPTER 5

CONCLUSION

The combined electrochemical and surface analysis of the library confirms that trimetallic NiFeCo catalyst shows superior catalytic activity to the bimetallic oxides due to its higher electronic conductivity, independently of the electrochemical surface area (Inamdar et al., 2020). We obtain an overpotential gain of 84 mV with the addition of ~4% cobalt to a bimetallic Ni−Fe oxide with 5% Fe. Our results demonstrate that the presence of a modest amount of cobalt has a significant effect on the OER activity. In the literature, the improvement in activity for Ni-Co-Fe oxide compared to Ni-Fe oxide was attributed to charge transfer effects from the cobalt component (Bates et al., 2016). Using a bifunctional edge-acceptor mechanism, Vandichel et al. explains that trimetallic (Fe, Co, Ni) catalysts outperform bimetallic OER catalysts (Vandichel et al., 2020). Also, Stevens et al. concluded that the most active OER catalysts were Ni-rich, containing 25− 40% iron and little to no cobalt (Stevens et al., 2019). On the contrary, our results contradict the reports on the benefits of Fe alone as a dopant, where better Tafel slopes and overpotentials were reported for $NiFeO_x$ compositions than $NiFeCoO_x$ (Smith et al., 2013). On account of these conflicting reports, we addressed the controversy by a systematic investigation involving a scrupulous comparative study of various combinations of multicomponent mixtures, gradually tending to the optimal composition.

To conclude, we successfully performed compositional space exploration of trimetallic Ni-Fe-Co oxide through combinatorial spray pyrolysis and OER scanning. The best performing ternary oxides were confined to the regions comprising 4−15% Fe, 4−15% Co, and 80−90% Ni. A low overpotential of 294 mV was achieved by $Ni_{91}Fe_5Co_4$ at a current density of 10 mA cm^{-2}. A doping level higher than 20% to nickel deteriorates the activity. The most optimal activity was achieved at a 5% doping of both Fe and Co to 90% nickel. This study provides a solid foundation for a systematic investigation of mixed-metal oxides, which could be extended to scrupulous comparative studies of new multimetallic systems involving other transition elements.

BSCF-Ag perovskite structure were synthesized to investigate its use as an OER electrocatalyst. We have found that silver doped BSCF perovskite structures show promising electrochemical performance for OER in basic media as a stable metal catalyst. Compared to undoped BSCF, BSCF-Ag perovskite structures showed better current density results in basic media for OER catalysis. Stability tests show that BSCF-Ag powder to have slightly lower potential values after 10 h, which demonstrates their stability in 1.0 M KOH solution. XRD and SEM results showed that desired structures were synthesized successfully. Increment at the surface area of the perovskite structure was determined with BET analysis, which is consistent with SEM images. The Tafel slope of BSCF-Ag was lower than pure BSCF, which concludes that BSCF-Ag has faster OER kinetics. Because of its better conductivity and higher surface area, BSCF-Ag was shown to improve OER activity. The factor adding to the improved OER performance for BSCF-Ag in respect to BSCF has been debated, which are faster charge transfer rate and, larger electrochemically active surface area. Future studies should be carried out to determine the exact mechanism.

REFERENCES

Abe, R., Higashi, M., & Domen, K. (2010). Facile Fabrication of an Efficient Oxynitride TaON Photoanode for Overall Water Splitting into H2 and O2 under Visible Light Irradiation. *Journal of the American Chemical Society, 132*(34), 11828-11829. doi:10.1021/ja1016552

Addamo, M., Augugliaro, V., Di Paola, A., García-López, E., Loddo, V., Marcì, G., . . . Schiavello, M. (2004). Preparation, Characterization, and Photoactivity of Polycrystalline Nanostructured TiO2 Catalysts. *The Journal of Physical Chemistry B, 108*(10), 3303-3310. doi:10.1021/jp0312924

Aleeva, Y., & Pignataro, B. (2014). Recent advances in upscalable wet methods and ink formulations for printed electronics. *Journal of Materials Chemistry C, 2*(32), 6436-6453. doi:10.1039/C4TC00618F

Alexander, B. D., Kulesza, P. J., Rutkowska, I., Solarska, R., & Augustynski, J. (2008). Metal oxide photoanodes for solar hydrogen production. *Journal of Materials Chemistry, 18*(20), 2298-2303. doi:10.1039/B718644D

Allison, I., Bindoff, N., Bindschadler, R., Cox, P., de Noblet, N., England, M. H., . . . Weaver, A. (2009). The Copenhagen Diagnosis.

Ananth, M. V., Manimaran, K., Arul Raj, I., & Sureka, N. (2007). Influence of air electrode electrocatalysts on performance of air-MH cells. *International Journal of Hydrogen Energy, 32*(17), 4267-4271. doi:https://doi.org/10.1016/j.ijhydene.2007.06.008

Anantharaj, S., Kennedy, J., & Kundu, S. (2017). Microwave-Initiated Facile Formation of Ni3Se4 Nanoassemblies for Enhanced and Stable Water Splitting in Neutral and Alkaline Media. *ACS Applied Materials & Interfaces, 9*(10), 8714-8728. doi:10.1021/acsami.6b15980

Balzarotti, R., Drago Ferrante, G., Italiano, C., Laganà, M., Francis, L. F., Vita, A., . . . Pino, L. (2022). RhNi/CeO2 catalytic activation of alumina open cell foams by dip-spin coating for the CO2 methanation of biogas. *Surface and Coatings Technology, 441*, 128563. doi:https://doi.org/10.1016/j.surfcoat.2022.128563

Bates, M. K., Jia, Q., Doan, H., Liang, W., & Mukerjee, S. (2016). Charge-Transfer Effects in Ni–Fe and Ni–Fe–Co Mixed-Metal Oxides for the Alkaline Oxygen Evolution Reaction. *ACS Catalysis, 6*(1), 155-161. doi:10.1021/acscatal.5b01481

Behrouzifar, A., Asadi, A. A., Mohammadi, T., & Pak, A. (2012). Experimental investigation and mathematical modeling of oxygen permeation through dense Ba0.5Sr0.5Co0.8Fe0.2O3−δ (BSCF) perovskite-type ceramic membranes. *Ceramics International, 38*(6), 4797-4811. doi:https://doi.org/10.1016/j.ceramint.2012.02.068

Berni, A., Mennig, M., & Schmidt, H. (2004). Doctor Blade. In M. A. Aegerter & M. Mennig (Eds.), *Sol-Gel Technologies for Glass Producers and Users* (pp. 89-92). Boston, MA: Springer US.

Bharathan, J., & Yang, Y. (1998). Polymer electroluminescent devices processed by inkjet printing: I. Polymer light-emitting logo. *Applied Physics Letters, 72*(21), 2660-2662. doi:10.1063/1.121090

Chatrchyan, S., Khachatryan, V., Sirunyan, A. M., Tumasyan, A., Adam, W., Bergauer, T., . . . Collaborations, T. (2014). Measurement of pseudorapidity distributions of charged particles in proton–proton collisions at $$\sqrt{s} = 8$$ TeV by the CMS and TOTEM experiments. *The European Physical Journal C, 74*(10), 3053. doi:10.1140/epjc/s10052-014-3053-6

Chen, D., Chen, C., Baiyee, Z. M., Shao, Z., & Ciucci, F. (2015). Nonstoichiometric Oxides as Low-Cost and Highly-Efficient Oxygen Reduction/Evolution Catalysts for Low-Temperature Electrochemical Devices. *Chemical Reviews, 115*(18), 9869-9921. doi:10.1021/acs.chemrev.5b00073

Chen, G., Zhou, W., Guan, D., Sunarso, J., Zhu, Y., Hu, X., . . . Shao, Z. Two orders of magnitude enhancement in oxygen evolution reactivity on amorphous Ba0.5Sr0.5Co0.8Fe0.2O3−δ nanofilms with tunable oxidation state. *Science Advances, 3*(6), e1603206. doi:10.1126/sciadv.1603206

Chen, Z., Ran, R., Zhou, W., Shao, Z., & Liu, S. (2007). Assessment of Ba0.5Sr0.5Co1−yFeyO3−δ (y=0.0–1.0) for prospective application as cathode for IT-SOFCs or oxygen permeating membrane. *Electrochimica Acta, 52*(25), 7343-7351. doi:https://doi.org/10.1016/j.electacta.2007.06.010

Cheng, X., Fabbri, E., Kim, B., Nachtegaal, M., & Schmidt, T. J. (2017). Effect of ball milling on the electrocatalytic activity of Ba0.5Sr0.5Co0.8Fe0.2O3 towards the oxygen evolution reaction. *Journal of Materials Chemistry A, 5*(25), 13130-13137. doi:10.1039/C7TA00794A

Compton, R. G., & Banks, C. E. (2007). *Understanding Voltammetry*: WORLD SCIENTIFIC.

Corrigan, D. A. (1987). The Catalysis of the Oxygen Evolution Reaction by Iron Impurities in Thin Film Nickel Oxide Electrodes. *Journal of The Electrochemical Society, 134*(2), 377-384. doi:10.1149/1.2100463

Cummins, G., & Desmulliez, M. P. Y. (2012). Inkjet printing of conductive materials: a review. *Circuit World, 38*(4), 193-213. doi:10.1108/03056121211280413

de Jongh, P. E., Vanmaekelbergh, D., & Kelly, J. J. (2000). Photoelectrochemistry of Electrodeposited Cu[sub 2]O. *Journal of The Electrochemical Society, 147*(2), 486. doi:10.1149/1.1393221

de Gans, B. J., Duineveld, P. C., & Schubert, U. S. (2004). Inkjet Printing of Polymers: State of the Art and Future Developments. *Advanced Materials, 16*(3), 203-213. doi:https://doi.org/10.1002/adma.200300385

Deganello, F., Liotta, L. F., Marcì, G., Fabbri, E., & Traversa, E. (2013). Strontium and iron-doped barium cobaltite prepared by solution combustion synthesis: exploring a mixed-fuel approach for tailored intermediate temperature solid oxide fuel cell cathode materials. *Materials for Renewable and Sustainable Energy, 2*(1), 8. doi:10.1007/s40243-013-0008-z

Derby, B. (2010). Inkjet Printing of Functional and Structural Materials: Fluid Property Requirements, Feature Stability, and Resolution. *Annual Review of Materials Research, 40*(1), 395-414. doi:10.1146/annurev-matsci-070909-104502

Druce, J., Téllez, H., Burriel, M., Sharp, M. D., Fawcett, L. J., Cook, S. N., . . . Kilner, J. A. (2014). Surface termination and subsurface restructuring of perovskite-based solid oxide electrode materials. *Energy & Environmental Science, 7*(11), 3593-3599. doi:10.1039/C4EE01497A

Duan, C., Kee, R. J., Zhu, H., Karakaya, C., Chen, Y., Ricote, S., . . . O'Hayre, R. (2018). Highly durable, coking and sulfur tolerant, fuel-flexible protonic ceramic fuel cells. *Nature, 557*(7704), 217-222. doi:10.1038/s41586-018-0082-6

Fabbri, E., Nachtegaal, M., Binninger, T., Cheng, X., Kim, B.-J., Durst, J., . . . Schmidt, T. J. (2017). Dynamic surface self-reconstruction is the key of highly active perovskite nano-electrocatalysts for water splitting. *Nature Materials, 16*(9), 925-931. doi:10.1038/nmat4938

Fabbri, E., Nachtegaal, M., Cheng, X., & Schmidt, T. J. (2015). Superior Bifunctional Electrocatalytic Activity of Ba0.5Sr0.5Co0.8Fe0.2O3-δ/Carbon Composite Electrodes: Insight into the Local Electronic Structure. *Advanced Energy Materials, 5*(17), 1402033. doi:https://doi.org/10.1002/aenm.201402033

Felix, C., Bladergroen, B. J., Linkov, V., Pollet, B. G., & Pasupathi, S. (2019). Ex-Situ Electrochemical Characterization of IrO2 Synthesized by a Modified Adams Fusion Method for the Oxygen Evolution Reaction. *Catalysts, 9*(4). doi:10.3390/catal9040318

Ferekides, C. S., Mamazza, R., Balasubramanian, U., & Morel, D. L. (2005). Transparent conductors and buffer layers for CdTe solar cells. *Thin Solid Films, 480-481*, 224-229. doi:https://doi.org/10.1016/j.tsf.2004.11.094

Feys, J., Vermeir, P., Lommens, P., Hopkins, S. C., Granados, X., Glowacki, B. A., . . . Van Driessche, I. (2012). Ink-jet printing of YBa2Cu3O7 superconducting coatings and patterns from aqueous solutions. *Journal of Materials Chemistry, 22*(9), 3717-3726. doi:10.1039/C1JM14899K

Fischer, D. W. (1972). X-Ray Band Spectra and Molecular-Orbital Structure of Rutile Ti${\mathrm{O}}_{2}$. *Physical Review B, 5*(11), 4219-4226. doi:10.1103/PhysRevB.5.4219

Fisher, C. A. J., Yoshiya, M., Iwamoto, Y., Ishii, J., Asanuma, M., & Yabuta, K. (2007). Oxide ion diffusion in perovskite-structured Ba1−xSrxCo1−yFeyO2.5: A molecular dynamics study. *Solid State Ionics, 177*(39), 3425-3431. doi:https://doi.org/10.1016/j.ssi.2006.03.060

Fominykh, K., Chernev, P., Zaharieva, I., Sicklinger, J., Stefanic, G., Döblinger, M., . . . Fattakhova-Rohlfing, D. (2015). Iron-Doped Nickel Oxide Nanocrystals as Highly Efficient Electrocatalysts for Alkaline Water Splitting. *ACS Nano, 9*(5), 5180-5188. doi:10.1021/acsnano.5b00520

Fortunato, E., Ginley, D., Hosono, H., & Paine, D. C. (2007). Transparent Conducting Oxides for Photovoltaics. *MRS Bulletin, 32*(3), 242-247. doi:10.1557/mrs2007.29

Friebel, D., Louie, M. W., Bajdich, M., Sanwald, K. E., Cai, Y., Wise, A. M., . . . Bell, A. T. (2015). Identification of Highly Active Fe Sites in (Ni,Fe)OOH for Electrocatalytic Water Splitting. *Journal of the American Chemical Society, 137*(3), 1305-1313. doi:10.1021/ja511559d

Fujishima, A., & Honda, K. (1972). Electrochemical Photolysis of Water at a Semiconductor Electrode. *Nature, 238*(5358), 37-38. doi:10.1038/238037a0

Gao, J., Meng, Y., Lee, S., Tong, J., & Brinkman, K. S. (2019). Effect of Infiltration of Barium Carbonate Nanoparticles on the Electrochemical Performance of La0.6Sr0.4Co0.2Fe0.8O3−δ Cathodes for Protonic Ceramic Fuel Cells. *JOM, 71*(1), 90-95. doi:10.1007/s11837-018-3098-3

Gebauer, J. S., Mackert, V., Ognjanović, S., & Winterer, M. (2018). Tailoring metal oxide nanoparticle dispersions for inkjet printing. *Journal of Colloid and Interface Science, 526*, 400-409. doi:https://doi.org/10.1016/j.jcis.2018.05.006

Gerken, J. B., Shaner, S. E., Massé, R. C., Porubsky, N. J., & Stahl, S. S. (2014). A survey of diverse earth abundant oxygen evolution electrocatalysts showing enhanced activity from Ni–Fe oxides containing a third metal. *Energy & Environmental Science, 7*(7), 2376-2382. doi:10.1039/C4EE00436A

Gilliam, R. J., Graydon, J. W., Kirk, D. W., & Thorpe, S. J. (2007). A review of specific conductivities of potassium hydroxide solutions for various concentrations and temperatures. *International Journal of Hydrogen Energy, 32*(3), 359-364. doi:https://doi.org/10.1016/j.ijhydene.2006.10.062

Gong, M., & Dai, H. (2015). A mini review of NiFe-based materials as highly active oxygen evolution reaction electrocatalysts. *Nano Research, 8*(1), 23-39. doi:10.1007/s12274-014-0591-z

Gordon, R. G. (2000). Criteria for Choosing Transparent Conductors. *MRS Bulletin, 25*(8), 52-57. doi:10.1557/mrs2000.151

Goto, K., Kawashima, T., & Tanabe, N. (2006). Heat-resisting TCO films for PV cells. *Solar Energy Materials and Solar Cells, 90*(18), 3251-3260. doi:https://doi.org/10.1016/j.solmat.2006.06.048

Görlin, M., Chernev, P., Ferreira de Araújo, J., Reier, T., Dresp, S., Paul, B., . . . Strasser, P. (2016). Oxygen Evolution Reaction Dynamics, Faradaic Charge Efficiency, and the Active Metal Redox States of Ni–Fe Oxide Water Splitting Electrocatalysts. *Journal of the American Chemical Society, 138*(17), 5603-5614. doi:10.1021/jacs.6b00332

Görlin, M., Ferreira de Araújo, J., Schmies, H., Bernsmeier, D., Dresp, S., Gliech, M., . . . Strasser, P. (2017). Tracking Catalyst Redox States and Reaction Dynamics in Ni–Fe Oxyhydroxide Oxygen Evolution Reaction Electrocatalysts: The Role of Catalyst Support and Electrolyte pH. *Journal of the American Chemical Society, 139*(5), 2070-2082. doi:10.1021/jacs.6b12250

Grimes, C. A., Varghese, O.K., Ranjan, S. (2008). *Light, Water, Hydrogen – The Solar Generation of Hydrogen by Water Photoelectrolysis*. New York: Springer.

Hauch, A., Küngas, R., Blennow, P., Hansen, A. B., Hansen, J. B., Mathiesen, B. V., & Mogensen, M. B. (2020). Recent advances in solid oxide cell technology for electrolysis. *Science, 370*(6513), eaba6118. doi:10.1126/science.aba6118

Heel, A., Holtappels, P., Hug, P., & Graule, T. (2010). Flame Spray Synthesis of Nanoscale La0.6Sr0.4Co0.2Fe0.8O3–δ and Ba0.5Sr0.5Co0.8Fe0.2O3–δ as Cathode Materials for Intermediate Temperature Solid Oxide Fuel Cells. *Fuel Cells, 10*(3), 419-432. doi:https://doi.org/10.1002/fuce.200900093

Hervieu, M. (1995). The Surface Science of Metal Oxides. By V. E. Henrich and P. A. Cox, Cambridge University Press, Cambridge 1994, XIV, 464 pp., hardcover, £ 55.00, ISBN 0–521–44389-X. *Advanced Materials, 7*(1), 91-92. doi:https://doi.org/10.1002/adma.19950070122

Hoffert Martin, I. (2010). Farewell to Fossil Fuels? *Science, 329*(5997), 1292-1294. doi:10.1126/science.1195449

Hon, K. K. B., Li, L., & Hutchings, I. M. (2008). Direct writing technology—Advances and developments. *CIRP Annals, 57*(2), 601-620. doi:https://doi.org/10.1016/j.cirp.2008.09.006

Hong, T., Chen, F., & Xia, C. (2015). Barium carbonate nanoparticle to enhance oxygen reduction activity of strontium doped lanthanum ferrite for solid oxide fuel cell. *Journal of Power Sources, 278*, 741-750. doi:https://doi.org/10.1016/j.jpowsour.2014.12.137

Hong, W. T., Risch, M., Stoerzinger, K. A., Grimaud, A., Suntivich, J., & Shao-Horn, Y. (2015). Toward the rational design of non-precious transition metal oxides for oxygen electrocatalysis. *Energy & Environmental Science, 8*(5), 1404-1427. doi:10.1039/C4EE03869J

Huang, Y.-L., Pellegrinelli, C., & Wachsman, E. D. (2017). Oxygen Dissociation Kinetics of Concurrent Heterogeneous Reactions on Metal Oxides. *ACS Catalysis, 7*(9), 5766-5772. doi:10.1021/acscatal.7b01096

Hung, I. M., & Laing, C.-Y. (2009). Synthesis and Characterization of Ba_{0.5}Sr_{0.5}Co_{0.8}Fe_{0.2}O_{3-δ} for Intermediate Temperature Solid Oxide Fuel Cell Cathode by Solid-State Reaction, Pechini and Citrate-EDTA Complexing Methods. *ECS Transactions, 25*(2), 2645-2650. doi:10.1149/1.3205823

Inamdar, A. I., Chavan, H. S., Pawar, S. M., Kim, H., & Im, H. (2020). NiFeCo oxide as an efficient and sustainable catalyst for the oxygen evolution reaction.

International Journal of Energy Research, 44(3), 1789-1797. doi:https://doi.org/10.1002/er.5026

Jia, L., He, G., Zhang, Y., Caro, J., & Jiang, H. (2021). Hydrogen Purification through a Highly Stable Dual-Phase Oxygen-Permeable Membrane. *Angewandte Chemie International Edition, 60*(10), 5204-5208. doi:https://doi.org/10.1002/anie.202010184

Jiang, H., & Tan, H. (2018). One Dimensional Model for Droplet Ejection Process in Inkjet Devices. *Fluids, 3*(2). doi:10.3390/fluids3020028

Jiang, S. P. (2007). Activation, microstructure, and polarization of solid oxide fuel cell cathodes. *Journal of Solid State Electrochemistry, 11*(1), 93-102. doi:10.1007/s10008-005-0076-9

Jung, W., & Tuller, H. L. (2012). Investigation of surface Sr segregation in model thin film solid oxide fuel cell perovskite electrodes. *Energy & Environmental Science, 5*(1), 5370-5378. doi:10.1039/C1EE02762J

Kato, H., & Kudo, A. (2002). Visible-Light-Response and Photocatalytic Activities of TiO2 and SrTiO3 Photocatalysts Codoped with Antimony and Chromium. *The Journal of Physical Chemistry B, 106*(19), 5029-5034. doi:10.1021/jp0255482

Kautkar, P. R., Shirbhate, S. C., & Acharya, S. A. (2018). Study on structural refinement and electrochemical behaviour of Ba0.5Sr0.5Co0.8Fe0.2O3−δ as cathode materials for intermediate temperature solid oxide fuel cells (IT-SOFC). *AIP Conference Proceedings, 1953*(1), 090057. doi:10.1063/1.5032904

Kay, A., Cesar, I., & Grätzel, M. (2006). New benchmark for water photooxidation by nanostructured alpha-Fe2O3 films. *J Am Chem Soc, 128*(49), 15714-15721. doi:10.1021/ja064380l

Khaselev, O., & Turner, J. A. (1998). A monolithic photovoltaic-photoelectrochemical device for hydrogen production via water splitting. *Science, 280*(5362), 425-427. doi:10.1126/science.280.5362.425

Kolb, G., & Hessel, V. (2004). Micro-structured reactors for gas phase reactions. *Chemical Engineering Journal, 98*(1), 1-38. doi:https://doi.org/10.1016/j.cej.2003.10.005

Kontos, A. I., Kontos, A. G., Tsoukleris, D. S., Vlachos, G. D., & Falaras, P. (2007). Superhydrophilicity and photocatalytic property of nanocrystalline titania sol–gel films. *Thin Solid Films, 515*(18), 7370-7375. doi:https://doi.org/10.1016/j.tsf.2007.02.082

Kralova, M., Dzik, P., Vesely, M., & Cihlar, J. (2014). Preparation and characterization of doped titanium dioxide printed layers. *Catalysis Today, 230*, 188-196. doi:https://doi.org/10.1016/j.cattod.2013.09.018

Kwon, H., Lee, W., & Han, J. W. (2016). Suppressing cation segregation on lanthanum-based perovskite oxides to enhance the stability of solid oxide fuel cell cathodes. *RSC Advances, 6*(74), 69782-69789. doi:10.1039/C6RA15253H

Landon, J., Demeter, E., İnoğlu, N., Keturakis, C., Wachs, I. E., Vasić, R., . . . Kitchin, J. R. (2012). Spectroscopic Characterization of Mixed Fe–Ni Oxide Electrocatalysts for the Oxygen Evolution Reaction in Alkaline Electrolytes. *ACS Catalysis, 2*(8), 1793-1801. doi:10.1021/cs3002644

Lee, W., Han, J. W., Chen, Y., Cai, Z., & Yildiz, B. (2013). Cation Size Mismatch and Charge Interactions Drive Dopant Segregation at the Surfaces of Manganite Perovskites. *Journal of the American Chemical Society, 135*(21), 7909-7925. doi:10.1021/ja3125349

Leo, A., Liu, S., & Diniz da Costa, J. C. (2009). The enhancement of oxygen flux on Ba0.5Sr0.5Co0.8Fe0.2O3−δ (BSCF) hollow fibers using silver surface modification. *Journal of Membrane Science, 340*(1), 148-153. doi:https://doi.org/10.1016/j.memsci.2009.05.022

Lewis, N. S., Crabtree, G., Nozik, A. J., Wasielewski, M. R., Alivisatos, P., Kung, H., . . . Nault, R. M. (2005). *Basic Research Needs for Solar Energy Utilization. Report of the Basic Energy Sciences Workshop on Solar Energy Utilization, April 18-21, 2005*. Retrieved from United States: https://www.osti.gov/biblio/899136

Lewis, N. S., & Nocera, D. G. (2006). Powering the planet: chemical challenges in solar energy utilization. *Proc Natl Acad Sci U S A, 103*(43), 15729-15735. doi:10.1073/pnas.0603395103 https://www.osti.gov/servlets/purl/899136

Li, X., He, L., Zhong, X., Zhang, J., Luo, S., Yi, W., . . . Xu, B. (2018). Evaluation of A-Site Ba²⁺-Deficient Ba<svg xmlns:xlink="http://www.w3.org/1999/xlink" xmlns="http://www.w3.org/2000/svg" style="vertical-align:-4.48895pt" id="M1" height="8.07707pt" version="1.1" viewBox="-0.0657574 -3.58812 20.888 8.07707" width="20.888pt"><g transform="matrix(.012,0,0,-0.012,0,4.134)"><path id="g50-50" d="M389 0V32C297 38 291 46 291 118V635C234 613 175 595 109 583V556L161 554C203 552 207 547 207 497V118C207 46 201 38 110 32V0H389Z"/></g><g transform="matrix(.012,0,0,-0.012,5.85,4.134)"><path id="g54-33" d="M556 236V289H56V236H556Z"/></g><g transform="matrix(.012,0,0,-0.012,13.189,4.134)"><path id="g50-121" d="M545 403C545 425 527 451 498 451C448 451 400 404 312 286L290 341C262 412 246 451 219 451C182 451 138 404 92 345L112 323C152 368 169 378 181 378C192 378 201 359 216 321L257 214C184 115 142 69 113 69C102 69 93 73 88 79S78 89 68 89C47 89 24 61 24 40C24 8 49 -12 75 -12C125 -12 175 31 271 175L312 64C330 15 357 -12 382 -12C421 -12 475 35 515 98L496 121C466 88 439 62 420 62C402 62 384 92 363 147L325 247C349 280 374 309 397 333C422 361 446 381 462 381C471 381 481 374 488 366C493 360 499 357 505 357C521 357 545 380 545 403Z"/></g></svg>Co_{0.4}Fe_{0.4}Zr_{0.1}Y_{0.1}O<svg xmlns:xlink="http://www.w3.org/1999/xlink" xmlns="http://www.w3.org/2000/svg" style="vertical-align:-4.48894pt" id="M2" height="8.95722pt" version="1.1" viewBox="-0.0657574 -4.46828 20.3575 8.95722" width="20.3575pt"><g transform="matrix(.012,0,0,-0.012,0,4.134)"><path id="g50-52" d="M290 377C321 398 342 415 358

430C378 450 389 473 389 502C389 578 329 635 238 635H237C184 635 137 610 109 578L64 515L88 493C112 529 154 573 208 573S303 542 303 482C303 409 233 370 141 341L149 308C165 313 190 319 215 319C272 319 341 283 341 193C342 98 292 43 222 43C163 43 122 72 96 94C88 101 79 100 70 94C61 87 47 73 46 60C44 47 48 37 62 23C76 10 118 -12 165 -12C238 -12 430 62 430 223C430 297 379 359 290 375V377Z"/></g><g transform="matrix(.012,0,0,-0.012,5.85,4.134)"><use xlink:href="#g54-33"/></g><g transform="matrix(.012,0,0,-0.012,13.189,4.134)"><path id="g50-226" d="M501 517C491 587 426 710 310 710C240 710 175 662 175 601C175 561 201 517 250 452C219 438 187 423 157 404C88 360 24 280 24 178C24 71 90 -12 195 -12C250 -12 297 6 334 32C412 87 452 170 452 249C452 335 408 396 333 481C259 565 229 601 229 621C229 642 245 652 275 652C359 652 427 583 490 499L501 517ZM364 233C364 142 323 33 222 33C173 33 119 81 119 178C119 265 156 335 193 374C213 395 242 413 272 425C308 384 364 319 364 233Z"/></g></svg> Oxides as Electrocatalysts for Efficient Hydrogen Evolution Reaction. *Scanning, 2018*, 1341608. doi:10.1155/2018/1341608

Li, X., Walsh, F. C., & Pletcher, D. (2011). Nickel based electrocatalysts for oxygen evolution in high current density, alkaline water electrolysers. *Physical Chemistry Chemical Physics, 13*(3), 1162-1167. doi:10.1039/C0CP00993H

Li, Y., Zhang, W., Zheng, Y., Chen, J., Yu, B., Chen, Y., & Liu, M. (2017). Controlling cation segregation in perovskite-based electrodes for high electro-catalytic activity and durability. *Chemical Society Reviews, 46*(20), 6345-6378. doi:10.1039/C7CS00120G

Li, Z., Fu, J.-Y., Feng, Y., Dong, C.-K., Liu, H., & Du, X.-W. (2019). A silver catalyst activated by stacking faults for the hydrogen evolution reaction. *Nature Catalysis, 2*(12), 1107-1114. doi:10.1038/s41929-019-0365-9

Liang, F., Zhou, W., Li, J., & Zhu, Z. (2013). Microwave-plasma induced reconstruction of silver catalysts for highly efficient oxygen reduction. *Journal of Materials Chemistry A, 1*(44), 13746-13749. doi:10.1039/C3TA13656F

Lin, Y., Ran, R., & Shao, Z. (2010). Silver-modified Ba0.5Sr0.5Co0.8Fe0.2O3−δ as cathodes for a proton conducting solid-oxide fuel cell. *International Journal of Hydrogen Energy, 35*(15), 8281-8288. doi:https://doi.org/10.1016/j.ijhydene.2009.12.017

Liu, P. F., Yin, H., Fu, H. Q., Zu, M. Y., Yang, H. G., & Zhao, H. (2020). Activation strategies of water-splitting electrocatalysts. *Journal of Materials Chemistry A, 8*(20), 10096-10129. doi:10.1039/D0TA01680B

Liu, R., Ye, K., Gao, Y., Zhang, W., Wang, G., & Cao, D. (2015). Ag supported on carbon fiber cloth as the catalyst for hydrazine oxidation in alkaline medium. *Electrochimica Acta, 186*, 239-244. doi:https://doi.org/10.1016/j.electacta.2015.10.126

Liu, X., Tarn, T.-J., Huang, F., & Fan, J. (2015). Recent advances in inkjet printing synthesis of functional metal oxides. *Particuology, 19*, 1-13. doi:https://doi.org/10.1016/j.partic.2014.05.001

Liu, Y., Zhu, X., Li, M., Liu, H., Cong, Y., & Yang, W. (2013). Stabilization of Low-Temperature Degradation in Mixed Ionic and Electronic Conducting Perovskite Oxygen Permeation Membranes. *Angewandte Chemie International Edition, 52*(11), 3232-3236. doi:https://doi.org/10.1002/anie.201209077

Louie, M. W., & Bell, A. T. (2013). An Investigation of Thin-Film Ni–Fe Oxide Catalysts for the Electrochemical Evolution of Oxygen. *Journal of the American Chemical Society, 135*(33), 12329-12337. doi:10.1021/ja405351s

Lu, J., Elam, J. W., & Stair, P. C. (2016). Atomic layer deposition—Sequential self-limiting surface reactions for advanced catalyst "bottom-up" synthesis. *Surface Science Reports, 71*(2), 410-472. doi:https://doi.org/10.1016/j.surfrep.2016.03.003

Lu, X., & Zhao, C. (2015). Electrodeposition of hierarchically structured three-dimensional nickel–iron electrodes for efficient oxygen evolution at high current densities. *Nature Communications, 6*(1), 6616. doi:10.1038/ncomms7616

Lyu, Z., Zhou, Y., Dai, W., Cui, X., Lai, M., Wang, L., . . . Chen, W. (2017). Recent advances in understanding of the mechanism and control of Li2O2 formation in aprotic Li–O2 batteries. *Chemical Society Reviews, 46*(19), 6046-6072. doi:10.1039/C7CS00255F

Ma, R., Lin, G., Zhou, Y., Liu, Q., Zhang, T., Shan, G., . . . Wang, J. (2019). A review of oxygen reduction mechanisms for metal-free carbon-based electrocatalysts. *npj Computational Materials, 5*(1), 78. doi:10.1038/s41524-019-0210-3

Ma, W., Ma, R., Wang, C., Liang, J., Liu, X., Zhou, K., & Sasaki, T. (2015). A Superlattice of Alternately Stacked Ni–Fe Hydroxide Nanosheets and Graphene for Efficient Splitting of Water. *ACS Nano, 9*(2), 1977-1984. doi:10.1021/nn5069836

Mahbubul, I. M., Saidur, R., & Amalina, M. A. (2012). Latest developments on the viscosity of nanofluids. *International Journal of Heat and Mass Transfer, 55*(4), 874-885. doi:https://doi.org/10.1016/j.ijheatmasstransfer.2011.10.021

Maleki, H., & Bertola, V. (2019). TiO2 Nanofilms on Polymeric Substrates for the Photocatalytic Degradation of Methylene Blue. *ACS Applied Nano Materials, 2*(11), 7237-7244. doi:10.1021/acsanm.9b01723

Maleki, H., & Bertola, V. (2020). Recent advances and prospects of inkjet printing in heterogeneous catalysis. *Catalysis Science & Technology, 10*(10), 3140-3159. doi:10.1039/D0CY00040J

Maric, R. (2008). Spray-based and CVD Processes for Synthesis of Fuel Cell Catalysts and Thin Catalyst Layers. In J. Zhang (Ed.), *PEM Fuel Cell Electrocatalysts and Catalyst Layers: Fundamentals and Applications* (pp. 917-963). London: Springer London.

Maruska, H. P., & Ghosh, A. K. (1979). Transition-metal dopants for extending the response of titanate photoelectrolysis anodes. *Solar Energy Materials, 1*(3), 237-247. doi:https://doi.org/10.1016/0165-1633(79)90042-X

Mattox, D. M. (2010). Chapter 1 - Introduction. In D. M. Mattox (Ed.), *Handbook of Physical Vapor Deposition (PVD) Processing (Second Edition)* (pp. 1-24). Boston: William Andrew Publishing.

May, K. J., Carlton, C. E., Stoerzinger, K. A., Risch, M., Suntivich, J., Lee, Y.-L., . . . Shao-Horn, Y. (2012). Influence of Oxygen Evolution during Water Oxidation on the Surface of Perovskite Oxide Catalysts. *The Journal of Physical Chemistry Letters, 3*(22), 3264-3270. doi:10.1021/jz301414z

McCrory, C. C. L., Jung, S., Peters, J. C., & Jaramillo, T. F. (2013). Benchmarking Heterogeneous Electrocatalysts for the Oxygen Evolution Reaction. *Journal of the American Chemical Society, 135*(45), 16977-16987. doi:10.1021/ja407115p

Mehla, S., Das, J., Jampaiah, D., Periasamy, S., Nafady, A., & Bhargava, S. K. (2019). Recent advances in preparation methods for catalytic thin films and coatings. *Catalysis Science & Technology, 9*(14), 3582-3602. doi:10.1039/C9CY00518H

Meille, V. (2006). Review on methods to deposit catalysts on structured surfaces. *Applied Catalysis A: General, 315*, 1-17. doi:https://doi.org/10.1016/j.apcata.2006.08.031

Minami, T. (2000). New n-Type Transparent Conducting Oxides. *MRS Bulletin, 25*(8), 38-44. doi:10.1557/mrs2000.149

Minami, T., Miyata, T., & Yamamoto, T. (1999). Stability of transparent conducting oxide films for use at high temperatures. *Journal of Vacuum Science & Technology A, 17*(4), 1822-1826. doi:10.1116/1.581897

Mohebi, M. M., & Evans, J. R. G. (2002). A Drop-on-Demand Ink-Jet Printer for Combinatorial Libraries and Functionally Graded Ceramics. *Journal of Combinatorial Chemistry, 4*(4), 267-274. doi:10.1021/cc010075e

Morozova, M., Kluson, P., Krysa, J., Dzik, P., Vesely, M., & Solcova, O. (2011). Thin TiO2 films prepared by inkjet printing of the reverse micelles sol–gel composition. *Sensors and Actuators B: Chemical, 160*(1), 371-378. doi:https://doi.org/10.1016/j.snb.2011.07.063

Mosiałek, M., Michna, A., Dziubaniuk, M., Bielańska, E., Kežionis, A., Šalkus, T., . . . Orliukas, A. F. (2018). Composite cathode material LSCF-Ag for solid oxide fuel cells obtained in one step sintering procedure. *Electrochimica Acta, 282*, 427-436. doi:https://doi.org/10.1016/j.electacta.2018.06.063

Nguyen, T.-T.-N., Chen, Y.-H., & He, J.-L. (2014). Preparation of inkjet-printed titanium monoxide as p-type absorber layer for photovoltaic purposes. *Thin Solid Films, 572*, 8-14. doi:https://doi.org/10.1016/j.tsf.2014.09.054

Norman, C., & Leach, C. (2011). In situ high temperature X-ray photoelectron spectroscopy study of barium strontium iron cobalt oxide. *Journal of Membrane Science, 382*(1), 158-165. doi:https://doi.org/10.1016/j.memsci.2011.08.006

Oliver-Tolentino, M. A., Vázquez-Samperio, J., Manzo-Robledo, A., González-Huerta, R. d. G., Flores-Moreno, J. L., Ramírez-Rosales, D., & Guzmán-Vargas, A.

(2014). An Approach to Understanding the Electrocatalytic Activity Enhancement by Superexchange Interaction toward OER in Alkaline Media of Ni–Fe LDH. *The Journal of Physical Chemistry C, 118*(39), 22432-22438. doi:10.1021/jp506946b

Oppenheim, J., & Beinhocker, E. D. (2009). *Climate change and the economy - myths versus realities*. Retrieved from Davos:

Osterloh, F. E. (2008). Inorganic Materials as Catalysts for Photochemical Splitting of Water. *Chemistry of Materials, 20*(1), 35-54. doi:10.1021/cm7024203

Othman, M. H. D., Droushiotis, N., Wu, Z., Kelsall, G., & Li, K. (2011). High-Performance, Anode-Supported, Microtubular SOFC Prepared from Single-Step-Fabricated, Dual-Layer Hollow Fibers. *Advanced Materials, 23*(21), 2480-2483. doi:https://doi.org/10.1002/adma.201100194

Pacala, S., & Socolow, R. (2004). Stabilization Wedges: Solving the Climate Problem for the Next 50 Years with Current Technologies. *Science, 305*(5686), 968-972. doi:10.1126/science.1100103

Pan, Y., Liu, Y., Zhao, J., Yang, K., Liang, J., Liu, D., . . . Liu, C. (2015). Monodispersed nickel phosphide nanocrystals with different phases: synthesis, characterization and electrocatalytic properties for hydrogen evolution. *Journal of Materials Chemistry A, 3*(4), 1656-1665. doi:10.1039/C4TA04867A

Park, C. Y., Lee, T. H., Dorris, S. E., Park, J. H., & Balachandran, U. (2012). Ethanol reforming using Ba0.5Sr0.5Cu0.2Fe0.8O3−δ/Ag composites as oxygen transport membranes. *Journal of Power Sources, 214*, 337-343. doi:https://doi.org/10.1016/j.jpowsour.2012.04.052

Perelaer, J., Smith, P. J., Mager, D., Soltman, D., Volkman, S. K., Subramanian, V., . . . Schubert, U. S. (2010). Printed electronics: the challenges involved in printing devices, interconnects, and contacts based on inorganic materials. *Journal of Materials Chemistry, 20*(39), 8446-8453. doi:10.1039/C0JM00264J

Piazza, F., Pavesi, L., Henini, M., & Johnston, D. (1992). Effect of As overpressure on Si-doped (111)A GaAs grown by molecular beam epitaxy: a photoluminescence study. *Semiconductor Science and Technology, 7*(12), 1504-1507. doi:10.1088/0268-1242/7/12/014

Rajeshwar, K., McConnell, R., Licht, S. (2008). *Solar Hydrogen Generation – Toward a Renewable Energy Future*. New York: Springer.

Raut, N. C., & Al-Shamery, K. (2018). Inkjet printing metals on flexible materials for plastic and paper electronics. *Journal of Materials Chemistry C, 6*(7), 1618-1641. doi:10.1039/C7TC04804A

Reis, N., & Derby, B. (2000). Ink Jet Deposition of Ceramic Suspensions: Modeling and Experiments of Droplet Formation. *MRS Online Proceedings Library, 624*(1), 65-70. doi:10.1557/PROC-624-65

Rodríguez-Gutiérrez, I., García-Rodríguez, R., Rodríguez-Pérez, M., Vega-Poot, A., Rodríguez Gattorno, G., Parkinson, B. A., & Oskam, G. (2018). Charge Transfer and Recombination Dynamics at Inkjet-Printed CuBi2O4 Electrodes for Photoelectrochemical Water Splitting. *The Journal of Physical Chemistry C, 122*(48), 27169-27179. doi:10.1021/acs.jpcc.8b07936

Ross, J. R. H. (2012). Chapter 1 - Heterogeneous Catalysis – Chemistry in Two Dimensions. In J. R. H. Ross (Ed.), *Heterogeneous Catalysis* (pp. 1-15). Amsterdam: Elsevier.

Rupp, G. M., Opitz, A. K., Nenning, A., Limbeck, A., & Fleig, J. (2017). Real-time impedance monitoring of oxygen reduction during surface modification of thin film cathodes. *Nature Materials, 16*(6), 640-645. doi:10.1038/nmat4879

Rupp, G. M., Téllez, H., Druce, J., Limbeck, A., Ishihara, T., Kilner, J., & Fleig, J. (2015). Surface chemistry of La0.6Sr0.4CoO3−δ thin films and its impact on the oxygen surface exchange resistance. *Journal of Materials Chemistry A, 3*(45), 22759-22769. doi:10.1039/C5TA05279C

Salvador, P. (1982). Analysis of the physical properties of TiO2・Be electrodes in the photoassisted oxidation of water. *Solar Energy Materials, 6*(2), 241-250. doi:https://doi.org/10.1016/0165-1633(82)90024-7

Santato, C., Odziemkowski, M., Ulmann, M., & Augustynski, J. (2001). Crystallographically Oriented Mesoporous WO3 Films: Synthesis, Characterization, and Applications. *Journal of the American Chemical Society, 123*(43), 10639-10649. doi:10.1021/ja011315x

Sato, S. (2002). Photocatalysts sensitive to visible light. *Science, 295*(5555), 626-627.

Sayama, K., Nomura, A., Arai, T., Sugita, T., Abe, R., Yanagida, M., . . . Sugihara, H. (2006). Photoelectrochemical decomposition of water into H2 and O2 on porous BiVO4 thin-film electrodes under visible light and significant effect of Ag ion treatment. *J Phys Chem B, 110*(23), 11352-11360. doi:10.1021/jp057539+

Schmalzried, H. (1964). F. A. Kröger: The Chemistry of Imperfect Crystals, North-Holland Publishing Company-Amsterdam 1964. 1039 Seiten. Preis: hfl. 110. *Berichte der Bunsengesellschaft für physikalische Chemie, 68*(6), 608-608. doi:https://doi.org/10.1002/bbpc.19640680615

Scoutaris, N., Alexander, M. R., Gellert, P. R., & Roberts, C. J. (2011). Inkjet printing as a novel medicine formulation technique. *Journal of Controlled Release, 156*(2), 179-185. doi:https://doi.org/10.1016/j.jconrel.2011.07.033

Seley, D., Ayers, K., & Parkinson, B. A. (2013). Combinatorial Search for Improved Metal Oxide Oxygen Evolution Electrocatalysts in Acidic Electrolytes. *ACS Combinatorial Science, 15*(2), 82-89. doi:10.1021/co300086h

Seo, C., Jang, D., Chae, J., & Shin, S. (2017). Altering the coffee-ring effect by adding a surfactant-like viscous polymer solution. *Scientific Reports, 7*(1), 500. doi:10.1038/s41598-017-00497-x

Shao, Z., & Haile, S. M. (2004). A high-performance cathode for the next generation of solid-oxide fuel cells. *Nature, 431*(7005), 170-173. doi:10.1038/nature02863

Shao, Z., Xiong, G., Tong, J., Dong, H., & Yang, W. (2001). Ba effect in doped Sr(Co0.8Fe0.2)O3-δ on the phase structure and oxygen permeation properties of the dense ceramic membranes. *Separation and Purification Technology, 25*(1), 419-429. doi:https://doi.org/10.1016/S1383-5866(01)00071-5

Singh, M., Haverinen, H. M., Dhagat, P., & Jabbour, G. E. (2010). Inkjet Printing—Process and Its Applications. *Advanced Materials, 22*(6), 673-685. doi:https://doi.org/10.1002/adma.200901141

Sirringhaus, H., & Shimoda, T. (2003). Inkjet Printing of Functional Materials. *MRS Bulletin, 28*(11), 802-806. doi:10.1557/mrs2003.228

Skorupska, K., Maggard, P. A., Eichberger, R., Schwarzburg, K., Shahbazi, P., Zoellner, B., & Parkinson, B. A. (2015). Combinatorial Investigations of High Temperature CuNb Oxide Phases for Photoelectrochemical Water Splitting. *ACS Combinatorial Science, 17*(12), 742-751. doi:10.1021/acscombsci.5b00142

Smith, R. D. L., Prévot, M. S., Fagan, R. D., Trudel, S., & Berlinguette, C. P. (2013). Water Oxidation Catalysis: Electrocatalytic Response to Metal Stoichiometry in Amorphous Metal Oxide Films Containing Iron, Cobalt, and Nickel. *Journal of the American Chemical Society, 135*(31), 11580-11586. doi:10.1021/ja403102j

Song, F., & Hu, X. (2014). Exfoliation of layered double hydroxides for enhanced oxygen evolution catalysis. *Nature Communications, 5*(1), 4477. doi:10.1038/ncomms5477

Stevens, M. B., Enman, L. J., Korkus, E. H., Zaffran, J., Trang, C. D. M., Asbury, J., . . . Boettcher, S. W. (2019). Ternary Ni-Co-Fe oxyhydroxide oxygen evolution catalysts: Intrinsic activity trends, electrical conductivity, and electronic band structure. *Nano Research, 12*(9), 2288-2295. doi:10.1007/s12274-019-2391-y

Stoyanov, E., Langenhorst, F., & Steinle-Neumann, G. (2007). The effect of valence state and site geometry on Ti L3,2 and O K electron energy-loss spectra of TixOy phases. *American Mineralogist, 92*(4), 577-586. doi:doi:10.2138/am.2007.2344

Suen, N.-T., Hung, S.-F., Quan, Q., Zhang, N., Xu, Y.-J., & Chen, H. M. (2017). Electrocatalysis for the oxygen evolution reaction: recent development and future perspectives. *Chemical Society Reviews, 46*(2), 337-365. doi:10.1039/C6CS00328A

Sun, Y., Liu, Z., Zhang, W., Chu, X., Cong, Y., Huang, K., & Feng, S. (2019). Unfolding B□O□B Bonds for an Enhanced ORR Performance in ABO3-Type Perovskites. *Small, 15*(29), 1803513. doi:https://doi.org/10.1002/smll.201803513

Sundriyal, P., & Bhattacharya, S. (2017). Inkjet-Printed Electrodes on A4 Paper Substrates for Low-Cost, Disposable, and Flexible Asymmetric Supercapacitors.

ACS Applied Materials & Interfaces, 9(44), 38507-38521. doi:10.1021/acsami.7b11262

Suntivich, J., Gasteiger, H. A., Yabuuchi, N., Nakanishi, H., Goodenough, J. B., & Shao-Horn, Y. (2011). Design principles for oxygen-reduction activity on perovskite oxide catalysts for fuel cells and metal–air batteries. *Nature Chemistry, 3*(7), 546-550. doi:10.1038/nchem.1069

Suntivich, J., May Kevin, J., Gasteiger Hubert, A., Goodenough John, B., & Shao-Horn, Y. (2011). A Perovskite Oxide Optimized for Oxygen Evolution Catalysis from Molecular Orbital Principles. *Science, 334*(6061), 1383-1385. doi:10.1126/science.1212858

Swierk, J. R., Klaus, S., Trotochaud, L., Bell, A. T., & Tilley, T. D. (2015). Electrochemical Study of the Energetics of the Oxygen Evolution Reaction at Nickel Iron (Oxy)Hydroxide Catalysts. *The Journal of Physical Chemistry C, 119*(33), 19022-19029. doi:10.1021/acs.jpcc.5b05861

Tian, Y., He, S., Liu, Y., Yang, C., Yang, R., Li, Y., . . . Pu, J. (2021). Comprehensive understanding of alkaline-earth elements effects on electrocatalytic activity and stability of LaFe0.8Ni0.2O3 electrode for high-temperature CO2 electrolysis. *Journal of CO2 Utilization, 53*, 101727. doi:https://doi.org/10.1016/j.jcou.2021.101727

Trotochaud, L., Young, S. L., Ranney, J. K., & Boettcher, S. W. (2014). Nickel–Iron Oxyhydroxide Oxygen-Evolution Electrocatalysts: The Role of Intentional and Incidental Iron Incorporation. *Journal of the American Chemical Society, 136*(18), 6744-6753. doi:10.1021/ja502379c

Turner, J., Aspinall, H. C., Rushworth, S., & Black, K. (2019). A hybrid nanoparticle/alkoxide ink for inkjet printing of TiO2: a templating effect to form anatase at 200 °C. *RSC Advances, 9*(67), 39143-39146. doi:10.1039/C9RA06119C

Vandichel, M., Busch, M., & Laasonen, K. (2020). Oxygen Evolution on Metal-oxy-hydroxides: Beneficial Role of Mixing Fe, Co, Ni Explained via Bifunctional Edge/acceptor Route. *ChemCatChem, 12*(5), 1436-1442. doi:https://doi.org/10.1002/cctc.201901951

Vollmann, H. W. (1980). New Technologies for the Filmless Manufacture of Printing Forms. *Angewandte Chemie International Edition in English, 19*(2), 99-110. doi:https://doi.org/10.1002/anie.198000991

Waasdorp, R., van den Heuvel, O., Versluis, F., Hajee, B., & Ghatkesar, M. K. (2018). Accessing individual 75-micron diameter nozzles of a desktop inkjet printer to dispense picoliter droplets on demand. *RSC Advances, 8*(27), 14765-14774. doi:10.1039/C8RA00756J

Wagner, N., Schulze, M., & Gülzow, E. (2004). Long term investigations of silver cathodes for alkaline fuel cells. *Journal of Power Sources, 127*(1), 264-272. doi:https://doi.org/10.1016/j.jpowsour.2003.09.022

Wang, A.-L., Xu, H., & Li, G.-R. (2016). NiCoFe Layered Triple Hydroxides with Porous Structures as High-Performance Electrocatalysts for Overall Water Splitting. *ACS Energy Letters, 1*(2), 445-453. doi:10.1021/acsenergylett.6b00219

Wang, T., Xu, W., & Wang, H. (2017). Ternary NiCoFe Layered Double Hydroxide Nanosheets Synthesized by Cation Exchange Reaction for Oxygen Evolution Reaction. *Electrochimica Acta, 257*, 118-127. doi:https://doi.org/10.1016/j.electacta.2017.10.074

Wang, Y., Zhang, B., Pan, W., Ma, H., & Zhang, J. (2017). 3 D Porous Nickel–Cobalt Nitrides Supported on Nickel Foam as Efficient Electrocatalysts for Overall Water Splitting. *ChemSusChem, 10*(21), 4170-4177. doi:https://doi.org/10.1002/cssc.201701456

Wei, B., Schroeder, M., & Martin, M. (2018). Surface Cation Segregation and Chromium Deposition on the Double-Perovskite Oxide PrBaCo2O5+δ. *ACS Applied Materials & Interfaces, 10*(10), 8621-8629. doi:10.1021/acsami.7b17881

Wen, Y., Zhang, C., He, H., Yu, Y., & Teraoka, Y. (2007). Catalytic oxidation of nitrogen monoxide over La1−xCexCoO3 perovskites. *Catalysis Today, 126*(3), 400-405. doi:https://doi.org/10.1016/j.cattod.2007.06.032

Won, S.-J., Kim, J. R., Suh, S., Lee, N.-I., Hwang, C. S., & Kim, H. J. (2011). Effect of Catalyst Layer Density and Growth Temperature in Rapid Atomic Layer Deposition of Silica Using Tris(tert-pentoxy)silanol. *ACS Applied Materials & Interfaces, 3*(5), 1633-1639. doi:10.1021/am200176j

Wörz, O., Jäckel, K. P., Richter, T., & Wolf, A. (2001). Microreactors – A New Efficient Tool for Reactor Development. *Chemical Engineering & Technology, 24*(2), 138-142. doi:https://doi.org/10.1002/1521-4125(200102)24:2<138::AID-CEAT138>3.0.CO;2-C

Wünscher, S., Abbel, R., Perelaer, J., & Schubert, U. S. (2014). Progress of alternative sintering approaches of inkjet-printed metal inks and their application for manufacturing of flexible electronic devices. *Journal of Materials Chemistry C, 2*(48), 10232-10261. doi:10.1039/C4TC01820F

Xia, Y. (2019). In My Element: Silver. *Chemistry – A European Journal, 25*(17), 4244-4244. doi:https://doi.org/10.1002/chem.201805675

Xiang, C., Suram, S. K., Haber, J. A., Guevarra, D. W., Soedarmadji, E., Jin, J., & Gregoire, J. M. (2014). High-Throughput Bubble Screening Method for Combinatorial Discovery of Electrocatalysts for Water Splitting. *ACS Combinatorial Science, 16*(2), 47-52. doi:10.1021/co400151h

Xiao, C., Lu, X., & Zhao, C. (2014). Unusual synergistic effects upon incorporation of Fe and/or Ni into mesoporous Co3O4 for enhanced oxygen evolution. *Chemical Communications, 50*(70), 10122-10125. doi:10.1039/C4CC04922E

Xu, X., Chen, Y., Zhou, W., Zhu, Z., Su, C., Liu, M., & Shao, Z. (2016). A Perovskite Electrocatalyst for Efficient Hydrogen Evolution Reaction. *Advanced Materials, 28*(30), 6442-6448. doi:https://doi.org/10.1002/adma.201600005

Xu, X., Pan, Y., Zhou, W., Chen, Y., Zhang, Z., & Shao, Z. (2016). Toward Enhanced Oxygen Evolution on Perovskite Oxides Synthesized from Different Approaches: A Case Study of Ba0.5Sr0.5Co0.8Fe0.2O3−δ. *Electrochimica Acta, 219*, 553-559. doi:https://doi.org/10.1016/j.electacta.2016.10.031

Yan, F., Wang, Y., Li, K., Zhu, C., Gao, P., Li, C., . . . Chen, Y. (2017). Highly Stable Three-Dimensional Porous Nickel-Iron Nitride Nanosheets for Full Water Splitting at High Current Densities. *Chemistry – A European Journal, 23*(42), 10187-10194. doi:https://doi.org/10.1002/chem.201701662

Yan, L., Cao, L., Dai, P., Gu, X., Liu, D., Li, L., . . . Zhao, X. (2017). Metal-Organic Frameworks Derived Nanotube of Nickel–Cobalt Bimetal Phosphides as Highly Efficient Electrocatalysts for Overall Water Splitting. *Advanced Functional Materials, 27*(40), 1703455. doi:https://doi.org/10.1002/adfm.201703455

Yang, L., Wang, S., Blinn, K., Liu, M., Liu, Z., Cheng, Z., & Liu, M. (2009). Enhanced Sulfur and Coking Tolerance of a Mixed Ion Conductor for SOFCs: BaZr0.1Ce0.7Y0.2–xYbxO3–δ. *Science, 326*(5949), 126-129. doi:10.1126/science.1174811

Yeo, B. S., & Bell, A. T. (2012). In Situ Raman Study of Nickel Oxide and Gold-Supported Nickel Oxide Catalysts for the Electrochemical Evolution of Oxygen. *The Journal of Physical Chemistry C, 116*(15), 8394-8400. doi:10.1021/jp3007415

Yin, Z., Huang, Y., Bu, N., Wang, X., & Xiong, Y. (2010). Inkjet printing for flexible electronics: Materials, processes and equipments. *Chinese Science Bulletin, 55*(30), 3383-3407. doi:10.1007/s11434-010-3251-y

Yin, Z., Sun, Y., Zhu, C., Li, C., Zhang, X., & Chen, Y. (2017). Bimetallic Ni–Mo nitride nanotubes as highly active and stable bifunctional electrocatalysts for full water splitting. *Journal of Materials Chemistry A, 5*(26), 13648-13658. doi:10.1039/C7TA02876H

Yu, J., Zhao, X., Zhao, Q., & Wang, G. (2001). Preparation and characterization of super-hydrophilic porous TiO2 coating films. *Materials Chemistry and Physics, 68*(1), 253-259. doi:https://doi.org/10.1016/S0254-0584(00)00364-3

Yu, X., Zhang, M., Yuan, W., & Shi, G. (2015). A high-performance three-dimensional Ni–Fe layered double hydroxide/graphene electrode for water oxidation. *Journal of Materials Chemistry A, 3*(13), 6921-6928. doi:10.1039/C5TA01034A

Yusop, U. A., Huai, T. K., Rahman, H. A., Baharuddin, N. A., & Raharjo, J. (2020). Electrochemical Performance of Barium Strontium Cobalt Ferrite -Samarium Doped Ceria- Argentum for Low Temperature Solid Oxide Fuel Cell. *Materials Science Forum, 991*, 94-100. doi:10.4028/www.scientific.net/MSF.991.94

Zhang, Y., Liu, J., Huang, X., Lu, Z., & Su, W. (2008). Low temperature solid oxide fuel cell with Ba0.5Sr0.5Co0.8Fe0.2O3 cathode prepared by screen printing. *Solid State Ionics, 179*(7), 250-255. doi:https://doi.org/10.1016/j.ssi.2008.02.008

Zhao, X., Fu, Y., Wang, J., Xu, Y., Tian, J.-H., & Yang, R. (2016). Ni-doped CoFe2O4 Hollow Nanospheres as Efficient Bi-functional Catalysts. *Electrochimica Acta, 201*, 172-178. doi:https://doi.org/10.1016/j.electacta.2016.04.001

Zhou, W., Ran, R., Shao, Z., Cai, R., Jin, W., Xu, N., & Ahn, J. (2008). Electrochemical performance of silver-modified Ba0.5Sr0.5Co0.8Fe0.2O3−δ cathodes prepared via electroless deposition. *Electrochimica Acta, 53*(13), 4370-4380. doi:https://doi.org/10.1016/j.electacta.2008.01.058

Zhou, Y., Lu, Q., Zhuang, Z., Hutchings, G. S., Kattel, S., Yan, Y., . . . Jiao, F. (2015). Oxygen Reduction at Very Low Overpotential on Nanoporous Ag Catalysts. *Advanced Energy Materials, 5*(13), 1500149. doi:https://doi.org/10.1002/aenm.201500149

Zhu, L., Wei, B., Wang, Z., Chen, K., Zhang, H., Zhang, Y., . . . Lü, Z. (2016). Electrochemically Driven Deactivation and Recovery in PrBaCo2O5+δ Oxygen Electrodes for Reversible Solid Oxide Fuel Cells. *ChemSusChem, 9*(17), 2443-2450. doi:https://doi.org/10.1002/cssc.201600658

Zhu, W. X., Lü, Z., Wang, L. X., Guan, X. Y., & Zhang, X. Y. (2011). Performance of Ba0.5Sr0.5Co0.8Fe0.2O3-δ-Ag Composite Cathode Materials for IT-SOFCs. *Advanced Materials Research, 311-313*, 2309-2314. doi:10.4028/www.scientific.net/AMR.311-313.2309

Zhu, Y., Zhou, W., & Shao, Z. (2017). Perovskite/Carbon Composites: Applications in Oxygen Electrocatalysis. *Small, 13*(12), 1603793. doi:https://doi.org/10.1002/smll.201603793

Zhu, Y., Zhou, W., Zhong, Y., Bu, Y., Chen, X., Zhong, Q., . . . Shao, Z. (2017). A Perovskite Nanorod as Bifunctional Electrocatalyst for Overall Water Splitting. *Advanced Energy Materials, 7*(8), 1602122. doi:https://doi.org/10.1002/aenm.201602122

Zhuang, S., Huang, K., Huang, C., Huang, H., Liu, S., & Fan, M. (2011). Preparation of silver-modified La0.6Ca0.4CoO3 binary electrocatalyst for bi-functional air electrodes in alkaline medium. *Journal of Power Sources, 196*(8), 4019-4025. doi:https://doi.org/10.1016/j.jpowsour.2010.11.056

VITA

Emre Yusuf GÖL

QUALIFICATION

- **PhD in Chemistry**

Izmir Institute of Technology – Izmir, Turkey

- **Master Program in Chemistry**

Yıldız Technical University – Istanbul, Turkey 2013-2015

- **Bachelor's Degree in Chemistry**

Yıldız Technical University – Istanbul, Turkey 2008-2013

- **High School**

Beşiktaş Atatürk Anatolian High School– Istanbul, Turkey 2004-2008

WORK EXPERIENCE

- **Research Assistant at Izmir Institute of Technology/** 2014-2022
  Projects

- **CTO at Ni-CAT Battery Technologies Inc.** 2020-Continues

Articles

- E. GOL, E. KARABUDAK MINI-REVIEW: "Ball-Type Phthalocyanines"; Similarities and Differences From Mono Phthalocyanines MINI-REVIEWS IN ORGANIC CHEMISTRY (2018)

- E. GOL, A. AYTEKİN, E. ÖZKAHRAMAN, E. KARABUDAK (2020). Investigation of oxygen evolution reaction performance of silver doped Ba0.5Sr0.5Co0.8Fe0.2O3-δ perovskite structure. JOURNAL OF APPLIED ELECTROCHEMISTRY